Advancements in Optical Properties of Thermochromic VO_2 Films through Experimental and Numerical Investigations

Mark J. Miller

A dissertation
submitted in partial fulfillment of the
requirements for the degree of

Doctor of Philosophy

University of Washington

2016

Reading Committee:

Junlan Wang (Chair)
Fumio Ohuchi
Minoru Taya
Jihui Yang (GSR)

Program Authorized to Offer Degree:

Department of Mechanical Engineering

University of Washington

Abstract

Advancements in Optical Properties of
Thermochromic VO_2 Films through
Experimental and Numerical Investigations

Mark J. Miller

Chair of the Supervisory Committee:
Professor Junlan Wang
Department of Mechanical Engineering

The Department of Energy reports that buildings consume more than 40% of primary energy in the U.S. and that this trend will continue for the foreseeable future. Furthermore, windows constitute a major path for energy losses from buildings and therefore also present a significant opportunity for efficiency improvement and waste reduction. With this in mind, the work in this dissertation is focused on improving the control of solar and thermal radiation through windows. These radiation spectra can be controlled independently because they peak at different wavelengths due to the much higher temperature (5500 °C) of the Sun compared to objects on Earth (25 °C). In this work, a thermochromic material is utilized to control solar irradiance and a low-emissive (low-E) material is used to control thermal radiation. Thermochromic materials possess optical properties that change in response to temperature and low-E coatings are

reflective in the mid-infrared (thermal) region. VO_2 is an exciting candidate for thermochromic coatings because its transmittance in the visible region is relatively constant, but its reflectance in the IR increases significantly with temperature. The main technical issues limiting VO_2 are luminous transmittance (T_{lum}) that is too low and a transition temperature (τ_c) that is too high. For the low-E coating, $(SnO_2)_x(In_2O_3)_{1-x}$ (ITO glass) was chosen because it has both high luminous transmittance and low emissivity.

In this dissertation it is shown that τ_c of VO_2 can be lowered from 50 to 45 °C by reducing the grain size of the film from 70 to 31 nm. In the area of luminous transmittance, TiO_2 is investigated as an anti-reflective coating which can be used to increase T_{lum}. Later in this work, it is demonstrated that the energy efficiency gained through VO_2 can be further improved by combining it with a low-E coating. The multilayer design combines anti-reflection in the visible region, thermochromism the near-IR and low emissivity in the mid-IR for an outstanding energy-efficient coating across the solar and thermal spectra. This dissertation contributes knowledge that helps reduce the barriers which currently limit thermochromic materials from being utilized for energy efficiency in built environments.

Table of Contents

List of Tables

List of Figures

Acknowledgements

Financial support was provided by the University of Washington Royalty Research Fund (grant no. 65-1984), Provost Bridge Fund, Clean Energy Institute, and Department of Mechanical Engineering. XRD, XPS, SEM, EDS, ellipsometry, AFM, and TEM characterizations were performed at the UW Molecular Analysis Facility, which is a member of the NSF National Nanotechnology Infrastructure Network. The furnace used in this work was accessed at the MSE User Facility. UV-Vis-NIR and FTIR spectrometry characterizations were performed using the core instrumentation of the Chemistry Department. The author would very much like to thank Profs. J. Wang (chair), J. Yang (GSR), F. Ohuchi, and M. Taya for serving on his supervisory committee. Above all, the author would like to acknowledge the invaluable leadership and guidance that his advisor, Prof. Junlan Wang, has provided during the course of this work.

Dedication

This work is dedicated to my loving and supportive family.

1 Introduction

1.1 Motivation

The Department of Energy reports that in 2011 approximately 41% of primary energy in the U.S. was used in residential and commercial buildings, as shown in Fig. 1.1 [1]. Given the strong demand for energy production as well as environmental issues such as global warming, a new path is needed for the 21st century and beyond. A balanced approach to meet this grand challenge comprises both a robust portfolio of energy-supply technologies as well as better utilization and efficiency of current energy production. One approach for improving energy efficiency in built environments is through the application of chromogenic (dynamic tint) coatings for windows.

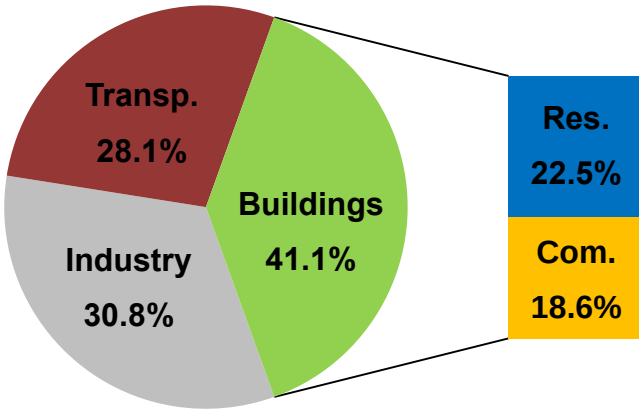

Fig. 1.1. Primary energy usage in the U.S. [1].

There are many different types of chromogenic technologies, and the three most popular are electrochromic, photochromic, and thermochromic [2-5]. These materials are briefly summarized in Table 1.1. Two important considerations for chromogenic devices are user controllability and production cost. The former can be thought of as either an advantage or disadvantage depending on user preferences and analysis criteria. Taking user controllability as a positive aspect, electrochromic devices have an advantage in this area. On the issue of production costs, clearly it

is desirable to reduce these as much as possible. Here thermochromic materials have an advantage since they only require a single layer and do not need energy input from the system (the heat for the optical transition comes from the Sun). Each of the technologies listed in Table 1.1 is promising and has various applications for which it is suitable. In this work, a thermochromic material, VO_2, is investigated.

Table 1.1. Background on chromogenic technologies [2-5].

Chromism	External Stimulus	Physical Mechanism	Example	Advantage	Disadvantage
Electro-	Applied Voltage	Reductive Intercalation	Li_xWO_3	User-controllable, demonstrated technology	Complexity, cost, need for electrical circuit
Photo-	Light Irradiation	Photo-reduction	AgCl	Simple, automatic	Loss of reversibility, not user-controllable
Thermo-	Temperature Change	Mott-Peierls* Transition	VO_2	Simple, inexpensive, automatic	τ_c currently too high, not user-controllable

* Mott Insulator: Material predicted to be conductive based on band theory, but is actually insulating due to interactions between electrons.

* Peierls Transition: Dimerization (pairing) of ions in a chain due to instability at low temperature.

1.2 TiO_2 as an Anti-reflective Coating

The primary focus of this dissertation is to gain fundamental insights on improving the performance of VO_2. One of the major issues for this material is insufficient luminous transmittance (less than 55%) [6]. A practical approach for improving T_{lum} is through anti-reflective coatings, such as TiO_2 [7]. For this reason TiO_2 will be briefly discussed in this section and then a parametric study on reactively-sputtered titania films will be presented in Ch. 2. A multilayer thin film with an anti-reflective TiO_2 layer will be presented in Ch. 5.

Titanium(IV) oxide is an important dielectric material with applications in optics, catalysis, and many other areas. It is utilized in a variety of forms including bulk, thin film, and nanoparticle [8]. Characteristic optical properties of the material comprise a high refractive index (2.5) and very wide band-gap (3.3 eV) [9]. TiO_2 has three naturally-occurring crystalline phases which are brookite (orthorhombic), anatase (tetragonal) and rutile (tetragonal). It is worth noting that rutile is the equilibrium phase and the other two are metastable. Thus brookite and anatase will convert to rutile given sufficient heat and time at atmospheric pressure. For the anti-reflective application desired in this dissertation, either anatase or rutile are suitable (brookite is a very uncommon polymorph).

Minimum reflection can be achieved in optical coatings when the incident and reflected waves are 180° out of phase. For a single interface, the Fresnel equations can be used to calculate the reflection coefficient. For complex multilayered systems, numerical techniques such as the transfer-matrix method are needed [10]. In this work, reflectance and transmittance are calculated with the program TFCalc by Software Spectra, Inc. The required inputs for the software are the refractive index and layer thickness of the material. Absorptance, transmittance and reflectance are the output from the program. The software has the capability to iterate layer thicknesses and re-run the analyses until user-specified goals are met. In this work, the goal is to have minimum reflectance in the visible region (400 to 700 nm). The layer thicknesses of the anti-reflective TiO_2 coatings in this dissertation were designed using this approach.

1.3 Structures, Properties and Applications of VO_2

VO_2 is a unique material that undergoes a reversible phase transition around 68 °C [11]. Below the critical temperature, τ_c, it is semiconducting with a monoclinic structure, and above τ_c it converts to a rutile tetragonal structure with metallic characteristics [12]. At the

semiconducting-to-metallic transition (SMT), properties such as electrical conductivity, magnetic susceptibility, optical transmittance and mechanical stiffness change abruptly [13-18]. From a fundamental standpoint this is an interesting phase transition with several details still being actively researched, and from an applications perspective there are numerous technologies that could benefit from such a material [19-24].

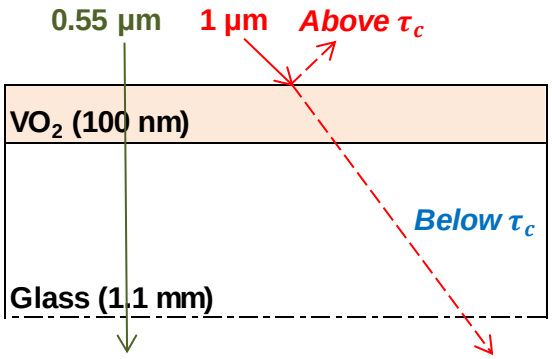

Fig. 1.2. Thermochromic smart window schematic showing luminous transmittance and near-infrared modulation.

Given that its optical properties change significantly and reversibly with temperature, VO_2 is a thermochromic material. Furthermore, its transmittance in the infrared (IR) region decreases substantially more than in the visible region when switched to the high-temperature metallic state. Since τ_c is relatively near room temperature, it is possible that a thin film of VO_2 could be used as a smart window coating by regulating solar irradiance. A schematic of a VO_2 smart window is shown in Fig. 1.2. The current technical challenge for this material is achieving a transition temperature near 25 °C while still maintaining adequate luminous transmittance and IR modulation. Doping the material with impurities such as W or Cr has been shown to drastically reduce τ_c; however, there is generally a tradeoff such that as τ_c is reduced, luminous transmittance decreases, IR modulation decreases or both decrease [6].

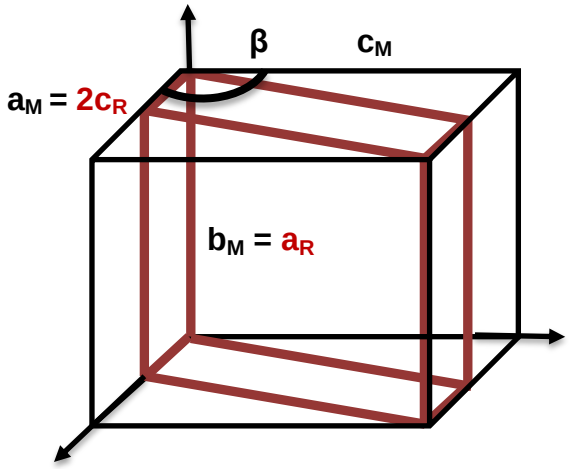

Fig. 1.3. Relationship between monoclinic (black line) and rutile (red line) VO_2 crystal lattices.

The lower temperature monoclinic (M1) phase is closely related to the higher temperature metallic rutile (R) phase, as shown in Fig. 1.3. Note that the angle β shown in Fig. 1.3 is 122.6° [25]. For this system, the M1 lattice has the space group $P2_1/c$ (No. 14), while the higher-symmetry R phase is $P4_2/mnm$ (No. 136). There is a shear distortion relation between the unit cells such that the monoclinic two-fold axis b_{M1} is parallel to the a-axis of the rutile structure [12]. The transformation matrix which relates these two structures was determined by Marezio et al. and is shown in Eqn. 1.1 [12].

$$\begin{pmatrix} a \\ b \\ c \end{pmatrix}_{M1} = \begin{pmatrix} 0 & 0 & 2 \\ 1 & 0 & 0 \\ 0 & 1 & \bar{1} \end{pmatrix} \begin{pmatrix} a \\ b \\ c \end{pmatrix}_{R} \tag{1.1}$$

From Eqn. 1.1, it can be seen that the monoclinic a-lattice parameter is twice that of the rutile c-parameter. Physically, this relationship corresponds to dimerized (paired) V atoms in the M1 structure forming a twisted configuration along the c-axis of the parent R structure [22]. Other VO_2 structures have also been reported in addition to the R and M1 phases [12].

The current understanding is that the transition temperature is related to the energy band structure of VO_2, and therefore one approach to modify τ_c is to dope the material with a suitable

cation, i.e. $M_xV_{1-x}O_2$. Ions such as W^{6+}, Mo^{6+}, Ta^{5+}, Nb^{5+} and Ru^{4+} are donor impurities which have been shown to lower the conduction band edge and corresponding τ_c of VO_2 [26]. Conversely, Ge^{4+}, Al^{3+} and Ga^{3+} are acceptor impurities which can introduce more holes into the valence band and increase τ_c if needed for a given design. However, it should be stated that this is only a working hypothesis in the literature, and the exact effects of dopants on τ_c are not entirely understood. For example, Manning et al. reported that in $W_{0.032}V_{0.968}O_2$ the charge state of W was 4+ [27], which does not entirely follow the trend described above. Furthermore, Mg^{2+} has been reported as lowering τ_c as well [28], and this appears to directly contradict the trend. Another possible explanation is the ratio of ionic radii of the dopant to the V^{4+}, but again the trend is not consistent for all dopants. The cause of the confusion may be due to combined effects such as the form of the material (i.e. bulk monocrystalline versus thin film), residual stress, non-stoichiometry, grain size and more.

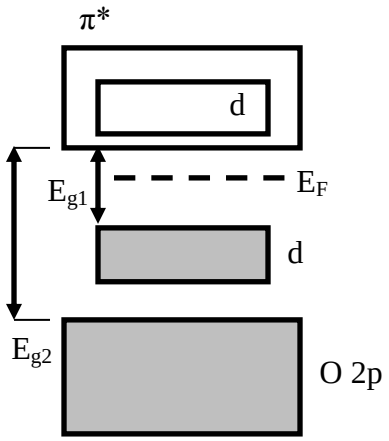

Fig. 1.4. Energy band diagram for VO_2 adapted from Wooten [29].

Doping VO_2 with Mg has been reported to increase the luminous transmittance of the material [28]. The mechanism for this is thought to be related to the energy band structure, which is shown in Fig. 1.4. As indicated in the figure, vanadium(IV) oxide has multiple band gaps.

Doping the structure with Mg may increase the second band-gap while leaving the first relatively constant. This is favorable for window coating applications because it increases the luminous transmittance [28]. An additional challenge that was identified through the course of this work is the diffusion of Na from soda lime glass into the film. This issue is discussed in detail and a practical solution for it is presented in Ch. 3.

1.4 Low Emissive Films

The purpose of VO_2 in this dissertation is to modulate the near-IR region of solar irradiance depending on the temperature of a built environment. It is also proposed that the energy efficiency of VO_2 can be enhanced by adding a low-emissive (low-E) layer which controls radiation in the "thermal" (mid-IR) region. The underlying principles of low-E coatings are as follows. Kirchhoff's radiation law states that the absorptance (α) of a perfect black-body is equal to its emissivity (ε) at a given wavelength. Now consider the conservation of energy for an irradiated surface: $\alpha + \rho + \tau = 1$, where ρ is reflectivity and τ is transmittance. For an opaque material τ is approximately zero. Furthermore since $\alpha = \varepsilon$, a high value of ρ is needed for a low-E surface. Stated simply, materials with high reflectivity possess low emissivity.

The solar and ambient thermal spectra can be controlled independently because their log-normal distributions peak at different wavelengths (0.5 and 10 μm, respectively). These distributions were calculated using the Planck equation for black-body radiation and the results are shown in Fig. 1.5. The figure shows clearly that the two distributions can be controlled independently using suitable materials.

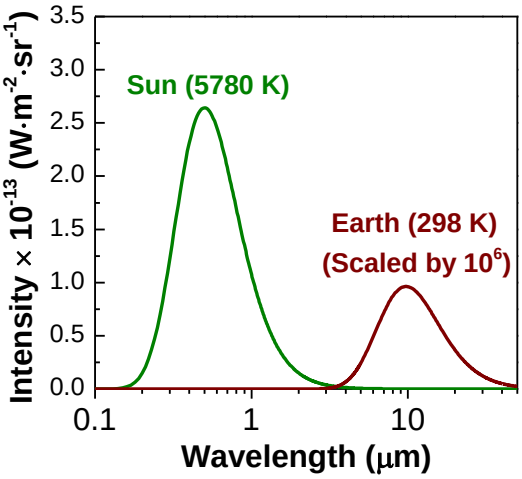

Fig. 1.5. Planck distributions for black-bodies at 5780 and 298 K, respectively.

When designed properly, low-E coatings possess high reflectance in the mid-IR and high transmittance in the visible region. One class of materials which exhibits these characteristics is transparent conducting oxides (TCOs). Other materials such as a thin film (i.e. 10 nm) of Ag can also be used, but then the layer must be sealed in an inert environment. Thus TCOs are both a high-performing and a more convenient option. A specific example is $(SnO_2)_x(In_2O_3)_{1-x}$, commonly referred to as ITO glass. A representative schematic of the coating is shown in Fig. 1.6. ITO glass has particularly favorable properties for the low-E application due to its exceptional luminous transmittance and mid-IR reflectance [30].

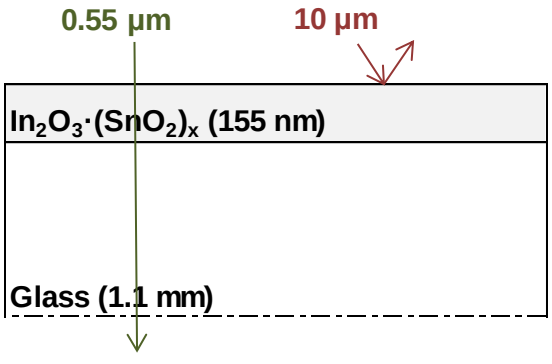

Fig. 1.6. Schematic of ITO as a low-E coating.

1.5 Research Objective

The over-arching goal of this work is to combine anti-reflective, thermochromic and low-E materials into a multilayer design with excellent energy-efficient properties across the UV, visible, and IR spectra. A schematic of the design is shown in Fig. 1.7. In the figure, *t* and *d* denote thickness and grain size, respectively. A layer thickness of 100 nm was chosen for VO_2 because it was found to produce a favorable combination of luminous transmittance and thermochromism. The 100 nm grain size limit is utilized because research has shown that τ_c can be reduced by limiting the grain size of VO_2 [18]. The 34 nm TiO_2 thickness was obtained by numerically optimizing the design for minimum reflectance in the visible region. More details on the optimization will be provided in Ch. 5. A 155 nm ITO layer is shown in Fig. 1.7 because this material was purchased from a manufacturer and this is the as-received thickness of the coating. Detailed discussion and results for the multilayer system will be presented in Ch. 5. The integration of these optical properties into a multilayer system is a significant step forward in energy-efficient coatings for windows in built environments.

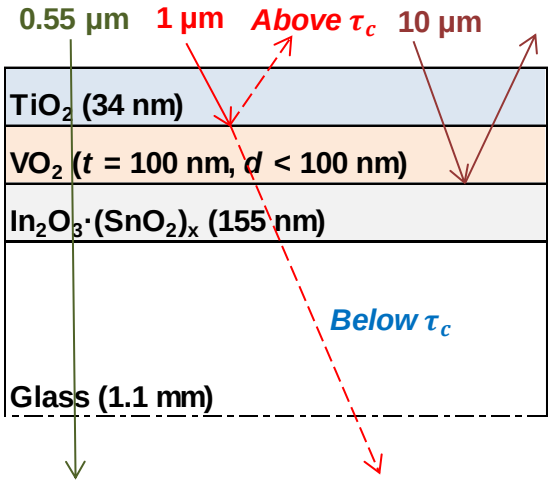

Fig. 1.7. Schematic of [ITO / VO_2 / TiO_2] multilayer system.

1.6 Organization of this Dissertation

Following this introduction, three chapters on individual layers of TiO_2 and VO_2 are presented. The work in Ch. 2 shows that the mechanical properties of TiO_2 can be controlled independently of the optical and electrical properties by varying synthesis temperature. This knowledge is important because TiO_2 is often used as the outer-most layer in optical devices including the thermochromic smart window investigated in this work. In Ch. 3, it is shown that substrate composition can have a very strong impact on the structure and properties of vanadium oxide thin films. Sodium (Na) in the glass can undesirably inhibit thermochromism; however, replacing half of the Na with potassium (K) suppresses the Na diffusion and promotes the nucleation of pure VO_2 with superior thermochromism. The work in Ch. 4 shows that the transition temperature of VO_2 can be lowered from 50 to 45 °C by reducing the effective grain size of the film from 70 to 31 nm. In Ch. 5, the multilayer system will be discussed in greater detail. The results show that low-E, thermochromic, and anti-reflective properties can be integrated into a single multilayer system. Furthermore, the transition temperature of the multilayer system can be controlled using the grain size approach investigated in Ch. 4.

2 Coupled Effects of Deposition and Annealing Temperatures on Optical, Electrical and Mechanical Properties of Titanium Oxide Thin Films

2.1 Overview

In this study the influence of deposition temperature and a post-deposition annealing process on the optical, electrical, mechanical, and tribological properties of titanium oxide thin films was investigated. Based on high-resolution XPS, it was observed that the films became more metallic as the deposition temperature was raised from 15 to 450 °C. Moreover, the mechanical and tribological properties of the film deposited at 450 °C were at least 50% greater than for the film deposited at 15 °C. After annealing at 450 °C for 30 mins in air, the films all became transparent and insulating. However, the annealing process had mixed effects on the mechanical and tribological properties such that the 15 and 250 °C films softened, but the 450 °C film hardened. This mixed trend is attributed to the different as-deposited film stoichiometries. The results show that the coupled effects of deposition temperature and post-deposition annealing are quite complex and that the mechanical properties of TiO_2 thin films can be controlled independently of their optical and electrical properties. This is important because TiO_2 coatings are often used as the outer-most layers in optical devices.

2.2 Introduction

Titanium(IV) oxide, also referred to as titania, is an important dielectric material with applications in optics, catalysis, and many other areas [31-37]. The thin film form of TiO_2 is particularly useful due to its high refractive index, photocatalytic functionality, hydrophilicity, and durability [31, 32, 38, 39]. There are numerous approaches for producing TiO_2 thin films which fall into categories comprising chemical vapor deposition (CVD), plating, sol-gel, and physical vapor deposition (PVD) [38, 40, 41]. One type of PVD, magnetron sputtering, is suitable for producing dense and smooth films with high purity [18]. Stoichiometric TiO_2 targets can be sputtered with an RF-powered plasma, or metallic Ti targets can be reactively-sputtered in a mixed environment of inert gas and O_2 using either RF or DC power [42-44].

Although the primary function of titania films is typically not structural, the mechanical and tribological properties of the material are nevertheless critical for system performance and reliability. This is especially true considering that TiO_2 films are often used as the outer-most layers in optical applications such as anti-reflective coatings [31]. The mechanical properties of TiO_2 films deposited on unheated substrates are well known and documented [45-48]. However, fewer studies have been performed on titania films grown at elevated temperatures. One study showed that increasing the deposition temperature from 25 to 300 ºC increased the wear resistance of the coatings [39]. Another study reported that the strength of room temperature-deposited TiO_2 films could be increased by annealing them at 300 ºC [49]. An earlier paper by Mayo et al. showed that the strength of nanophase titania could be increased by sintering the material at up to 900 ºC [50]; however, it should be noted that this is a different form of the material compared to the continuous thin film form of TiO_2. These studies raise the question "What is the interplay and combined effect of both elevated deposition temperature and post-deposition annealing on the mechanical and tribological properties of titanium oxide thin films?"

This seemingly simple question is actually non-trivial due to complex mechanisms such as film densification, grain growth, residual stress, non-stoichiometry, and more.

To answer the aforementioned question, titanium oxide thin films were deposited with three different substrate temperatures and subsequently annealed in air. The chemical composition and optical, electrical and mechanical properties of the films were systematically characterized. It was found that the mechanical and tribological properties of the samples improved by 50% or more as the deposition temperature was raised from 15 to 450 °C. This was attributed to film densification. The post-deposition annealing process had mixed effects on the mechanical properties, such that the 15 and 250 °C films softened but the 450 °C film hardened. These mixed effects were attributed to stoichiometric differences at the start of the annealing process (the 450 °C film was more metallic), as well as a reduction in the residual stresses in the films. The results show that the combined effects of deposition temperature and post-deposition annealing are quite complex and that the mechanical properties of TiO_2 thin films can be controlled independently of their optical and electrical properties.

2.3 Experimental Procedure

Thin titanium oxide films were deposited on 1 mm thick glass substrates by reactively sputtering a 99.995% pure Ti target (50.8 mm diameter × 6.35 mm thickness) in a mixed Ar + O_2 environment using an Orion 5 UHV magnetron sputtering system (AJA International, Inc.). The films were deposited at substrate temperatures of 15, 250, and 450 °C, respectively, using a PID controller with feedback from a Type K thermocouple. The deposition power was 150 W and the distance between target and substrate was approximately 130 mm. Ar and O_2 flow rates were 20 and 1 sccm, respectively, and absolute deposition pressure was 1.16 Pa. These conditions

resulted in a deposition rate of approximately 7.33 $nm \cdot min^{-1}$. Each of the deposition processes was carried out for 75 mins, which resulted in a nominal film thickness of 550 nm. The process was controlled carefully since the structure and properties of reactively-sputtered thin films are known to rely strongly on the processing conditions [51]. After deposition, samples were annealed in quiescent air at 450 °C for 30 mins using a Barnstead Thermolyne 47900 furnace. The 450 °C annealing temperature was chosen based on a series of parametric studies. This temperature was found to be high enough to induce the amorphous-to-crystalline transition of the titanium oxide film, yet still below the melting temperature (700 ºC) of the glass substrate.

The thickness of the films was measured using the scanning probe microscopy (SPM) function of a Ubi1 nanomechanical test instrument (Hysitron, Inc.). The chemical compositions of the samples were characterized with high-resolution X-ray photoelectron spectroscopy (XPS) using a Surface Science Instruments S-Probe. Monochromatic Al K_α was used as the radiation source for XPS, and the data was analyzed with CasaXPS 2.3.15. The spectra were corrected by setting the C 1s binding energy at 284.6 eV, which is a standard practice for XPS analysis [52].

Microstructures of the samples were characterized with X-ray diffraction (XRD) using a Bruker D8 Discover with GADDS. Cu K_α was used as the radiation source for XRD, and data was collected from 2θ of 15 to 70°. Naturally-fractured cross sections of the samples were characterized with a Sirion FEI scanning electron microscope (SEM) in secondary electron detection mode. This technique elucidated the microstructure and also provided a means to verify the thickness of the films. Optical transmittance was obtained with UV-Vis-NIR spectrophotometry using a Varian Cary 5000. The measurement was performed between wavelengths of 250 and 2500 nm. Electrical resistivities of the samples were determined with the 4-point probe technique using a Keithley 2400 SourceMeter and 2182 NanoVoltmeter. Electrical

contacts were connected to the films with silver paste. Nanoindentation and nanoscratch characterizations were performed on the films using a Hysitron Ubi1 nanomechanical test instrument. The procedure in this work enabled a systematic study of the influence of synthesis temperature on the composition and microstructure, and optical, electrical, and mechanical properties of reactively-sputtered titanium oxide thin films.

2.4 Results and Discussion

The compositions of the titanium oxide films were determined with high-res XPS, and the results are shown in Fig. 2.1. All films are shown to have a TiO_x composition, and x was observed to decrease as the deposition temperature was raised from 15 to 450 °C. This can be seen in Fig. 2.1 as the percentage of Ti^{3+} increased from 0 to 15% due to the increase in deposition temperature. The stoichiometries of the as-deposited films were approximately TiO_2, $TiO_{1.96}$ and $TiO_{1.92}$, respectively based on the deconvolution of the Ti $2p_{3/2}$ binding energy into Ti^{4+} and Ti^{3+} curves. The reason for the increase in metallic content may have been an increase in sputter rate associated with a decrease in target poisoning. During reactive sputtering, an insulating layer builds up on the surface of the target which results in a decreased sputter rate. This effect is known as target poisoning, and in the current study it appears to have been somewhat offset by the increase in deposition temperature. Following the deposition process, the films were annealed in air and fully oxidized into TiO_2. This can be inferred from Fig. 2.1 since the percentage of Ti^{3+} of each of the annealed films was 0%.

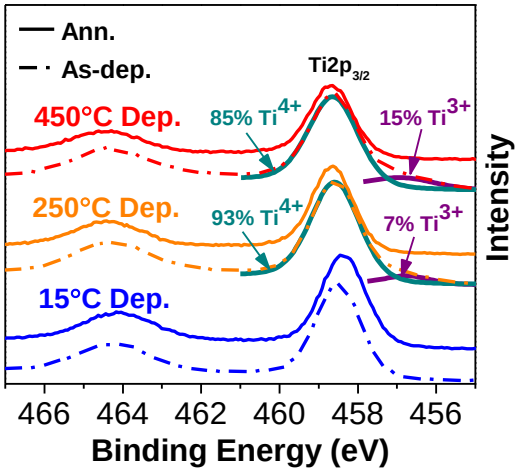

Fig. 2.1. XPS spectra for as-deposited and annealed TiO_x films.

The XRD results shown in Fig. 2.2 reveal that the as-deposited films were all amorphous. After annealing the films crystallized into the anatase TiO_2 structure (space group $I\,4_1/a\,m\,d$; no. 141) [53, 54], although the intensity of the XRD peaks was inversely related to the deposition temperature. Additionally, several anatase peaks were observed for the 15 °C-dep/450 °C-ann film that were not observed for the films deposited at 250 and 450 °C. The reason for this inverse relationship may have been the suboxide stoichiometry reported in Fig. 2.1. The 15 °C film needed energy only to crystallize, whereas the 450 °C film needed energy to both oxidize and crystallize. Thus the 450 °C sample would have required more time to obtain both the stoichiometry and microstructure of the low temperature film.

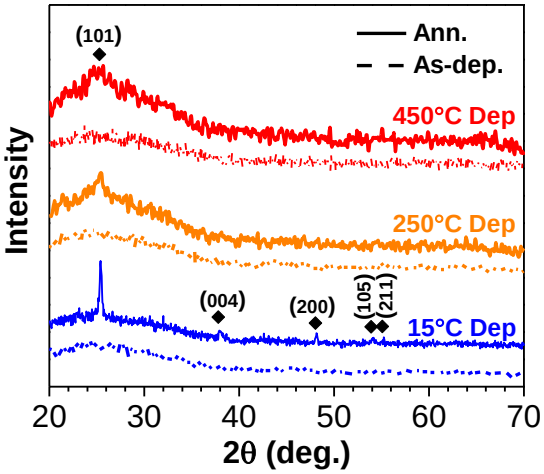

Fig. 2.2. XRD spectra for as-deposited and annealed TiO_x films.

Naturally-fractured cross sections of the TiO_x films were characterized with SEM, and the results are shown in Fig. 2.3. The images confirm that the thickness of the films was approximately 550 nm. All three as-deposited samples consisted of high aspect ratio nanoclusters perpendicular to the substrate. Fine voids were also present in the structures, although in general the films were uniform and smooth. After annealing, the 15 °C film transitioned to a somewhat equiaxed state, whereas the 250 and 450 °C films retained their columnar-like structures.

After characterizing the composition and structure of the films, the optical transmittance and band gaps were determined with UV-Vis-NIR spectrophotometry. It was observed that the transmittance of the samples decreased with increasing deposition temperature, as shown in Fig. 2.4(a). After annealing, the films became fully transparent in the visible and near-IR regions, which is shown in Fig. 2.4(b). The reason for this increased transmittance is the oxidation and crystallization that occurred during the annealing process. Optical band gaps, E_g, of the samples were determined using the following relationship:

$$\alpha h\nu = \alpha_0 \left(h\nu - E_g\right)^2 \tag{2.1}$$

where α is the measured absorption coefficient from the UV-Vis-NIR measurement, h is Planck's constant, ν is the frequency of the light, and α_0 is a material-specific constant [55]. E_g was calculated by plotting $\sqrt{\alpha}$ versus photon energy $(h\nu)$ and extrapolating a linear fit at the spike in absorption. A representative plot is shown in Fig. 2.5 for the 15 °C-dep/450 °C-ann sample. The band gap of the sample is calculated to be approximately 3.38 eV, which means that it is transparent in the visible region (3.1 to 1.7 eV) but opaque in the UV (5.0 to 3.1 eV). These optical properties are characteristic of crystalline TiO_2. Band gaps for each of the films are provided in Table 2.1. The results show that E_g decreased from 3.23 to 2.82 eV as the deposition temperature was raised from 15 to 450 °C. The narrower band gaps of the 250 and 450 °C samples were attributed to the suboxide stoichiometries shown in Fig. 2.1. After annealing, the films reached complete TiO_2 stoichiometry and the band gap of each sample was greater than 3.18 eV. Thus each annealed film was fully transparent in the visible region.

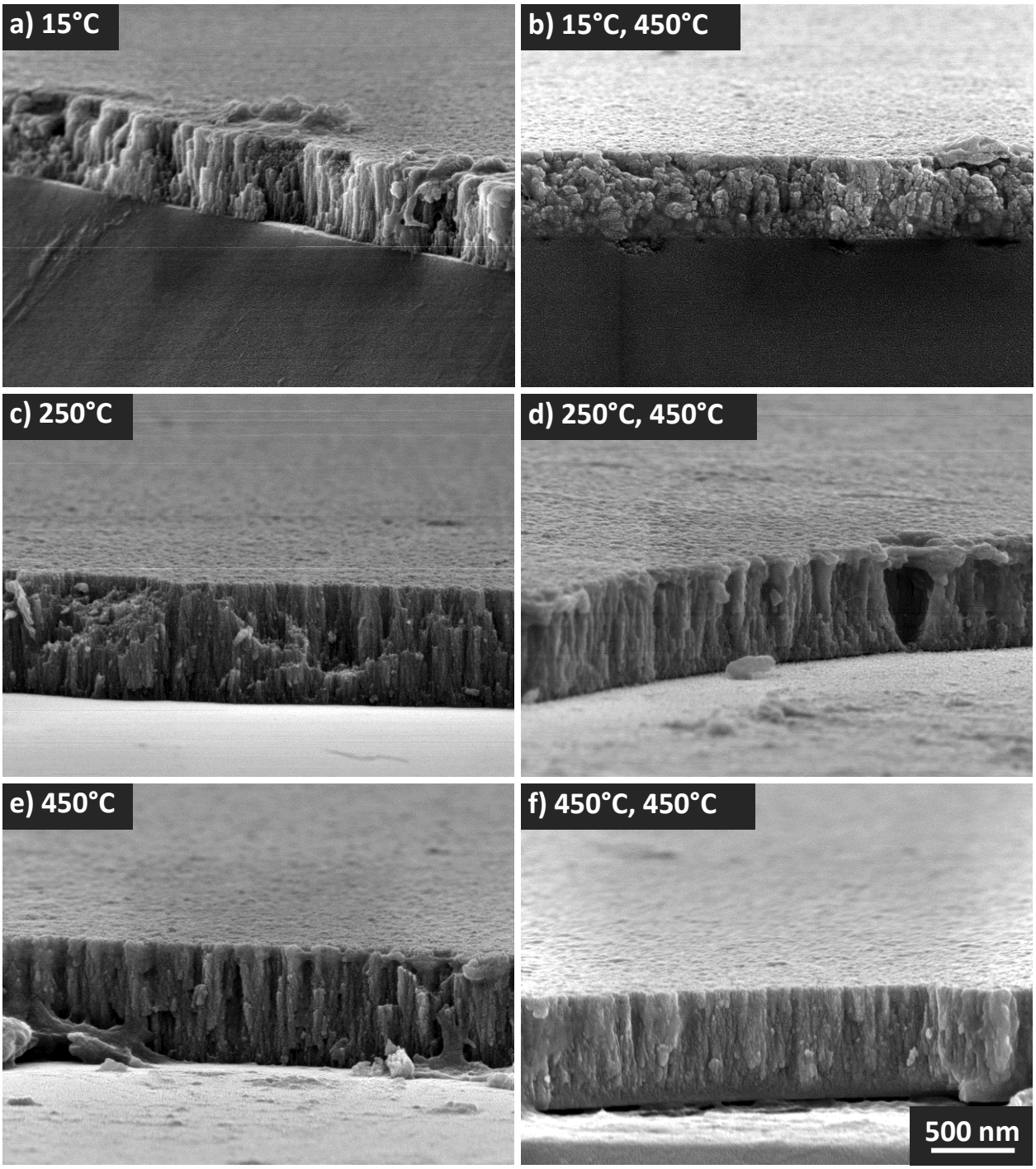

Fig. 2.3. SEM images of TiO_x films before annealing (a, c, e) and after annealing (b, d, f) at 450 °C for 30 mins in air. The 500 nm scale bar applies equally for each image.

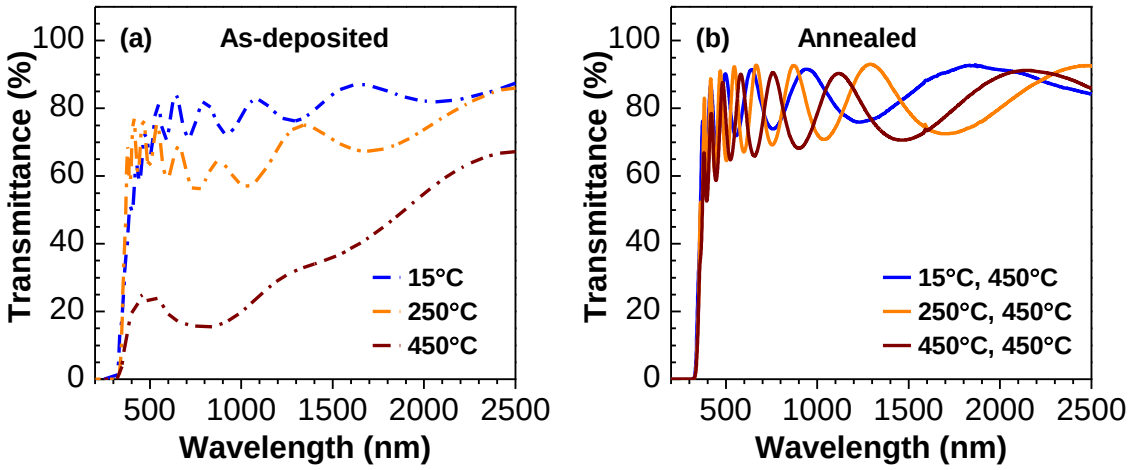

Fig. 2.4. Optical transmittance of TiO_x films before annealing (a) and after annealing (b).

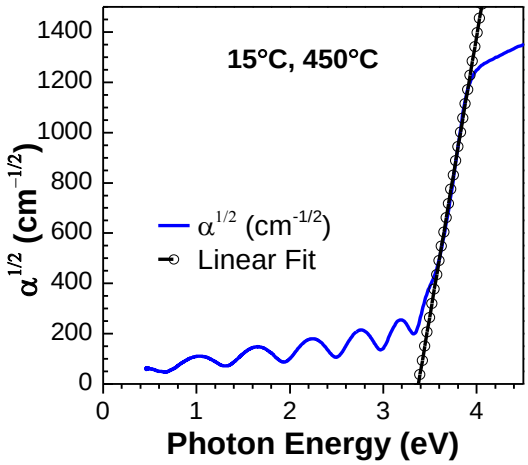

Fig. 2.5. Representative linear extrapolation technique used to determine band gaps of TiO_x films.

Table 2.1. Optical band gaps of TiO_x films before and after annealing.

TiO_x Film	E_g (eV)
15 °C-dep.	3.23
250 °C-dep.	3.22
450 °C-dep.	2.82
15 °C-dep., 450 °C-ann.	3.38
250 °C-dep., 450 °C-ann.	3.30
450 °C-dep., 450 °C-ann.	3.18

The trend of decreasing oxidation with increasing deposition temperature was supported through electrical resistivity characterizations, as shown in Fig. 2.6. Based on four-point probe measurements, the resistivity of the samples decreased four orders of magnitude from 20000 to 1 Ω·cm as the deposition temperature was raised from 15 to 450 °C. These results show that the reduction of the Ti^{4+} in the film caused a significant increase in conductivity. After annealing, the resistivity of each film was at least 20000 Ω·cm. This large value of resistivity is consistent with the wide optical band gaps reported in Table 2.1, and therefore each film was both transparent and insulating after annealing.

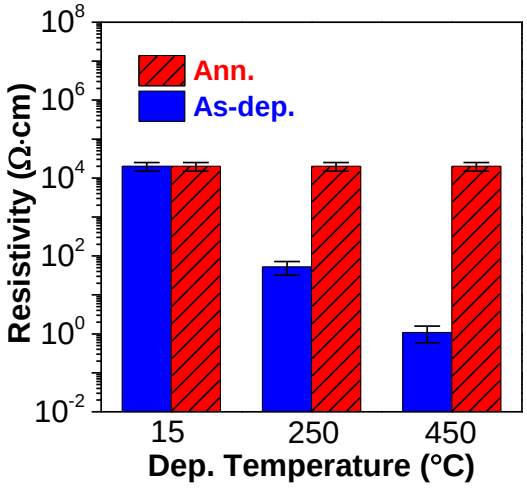

Fig. 2.6. Electrical resistivity of TiO_x films obtained with 4-point probe technique.

One of the primary goals of this work was to determine how synthesis temperature affects the mechanical properties of titanium oxide thin films. To answer this question, the reduced modulus and hardness of the samples were determined with nanoindentation using a Hysitron Ubi1 nanomechanical test instrument. An array of 16 indents per sample was performed with a Berkovich tip. The loading function was a 10-5-10 sec trapezoidal routine. The loading range

was 150 to 750 μN, which resulted in an indentation depth of up to 80 nm. This depth was approximately 15% of the 550 nm film thickness. The mechanical properties were determined using the method of Oliver and Pharr [56]. Briefly, the reduced modulus (E_r) was measured by taking the slope of the upper portion of the unloading curve, as described by Eqn. (2.2). Here $S = dP/dh$ is the measured stiffness from the unloading curve, P is the indentation load and h is the indentation depth.

$$E_r = \frac{S}{2}\sqrt{\frac{\pi}{A}} = \frac{1}{2}\sqrt{\frac{\pi}{A}}\left(\frac{dP}{dh}\right) \tag{2.2}$$

The reduced modulus is related to the sample and indenter properties as shown below in Eqn. (2.3).

$$\frac{1}{E_r} = \frac{1-\nu^2}{E} + \frac{1-\nu_i^2}{E_i} \tag{2.3}$$

The properties ν and E are Poisson's ratio and the elastic modulus of the specimen. The properties of the diamond nanoindenter tip, ν_i and E_i, are 0.07 and 1140 GPa, respectively. Sample hardness (H) is determined by dividing the maximum load by the contact area, as shown in Eqn. (2.4).

$$H = \frac{P_{max}}{A} \tag{2.4}$$

The nanoindentation results, provided in Fig. 2.7, show that the mechanical properties increased significantly as the deposition temperature was raised from 15 to 450 °C. E_r increased from 79 ± 10 to 109 ± 5 GPa and H increased from 3.2 ± 0.3 to 6.2 ± 0.3 GPa. The reason for this strengthening may have been an increase in film density due to the higher synthesis temperature. Post-deposition annealing had mixed effects on the mechanical properties of the samples. The modulus of the 15 and 250 °C films decreased by 2 GPa and the hardness decreased by about 1 GPa after the samples were annealed. This reduction in strength may have

been the result of relaxation in residual stresses from the deposition process. By contrast, E_r increased for the 450 °C film to 126 ± 15 GPa and H increased to 7.0 ± 1.4 GPa. The increase in strength for the 450 °C sample may have been due to the increased oxidation shown in Fig. 2.1. The mixed effects of the annealing process are most likely due to the different initial stoichiometries of the TiO_x films. The compositions of the as-deposited films were approximately TiO_2, $TiO_{1.96}$, and $TiO_{1.92}$, based on the high-res XPS results shown in Fig. 2.1. Since the 450 °C film ($TiO_{1.92}$) required the most time for oxidation and crystallization, it may not have had sufficient time in the annealing process to undergo the relaxation mechanisms of the 15 °C (TiO_2) and 250 °C ($TiO_{1.96}$) films.

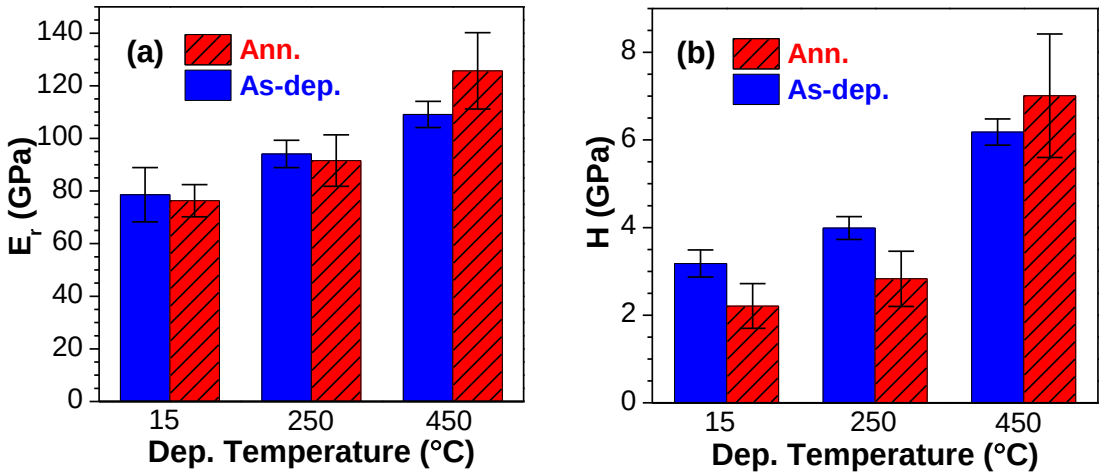

Fig. 2.7. Reduced modulus (a) and hardness (b) of films before annealing (solid) and after annealing (cross-hatched).

Wear resistance of the samples was characterized by performing nanoscratch tests on the film surfaces. A constant load of 500 μN was applied as the Berkovich tip translated 8 μm across the films. Each sample was tested 3 times. SPM topographies of the scratches, shown in Fig. 2.8, agree very closely with the hardness results presented in Fig. 2.7(b). Wear resistance increased with deposition temperature, and then the post-deposition anneal had mixed effects on the

tribological properties. The 450 °C-dep/450 °C-ann film had the best wear resistance of all of the samples. Scratch profiles along the scratch direction are provided in Fig. 2.9. The results show that the scratch depth was 32 nm for the 15 °C film but only 13 nm for the 450 °C film. After annealing, the scratch depth increased to 42 nm for the 15 °C film, but was nearly constant at 15 nm for the 450 °C sample. In addition to wear resistance, the coefficient of friction (μ_k) was determined from the scratch tests. μ_k is defined as the ratio of the lateral to normal force. The results, presented in Fig. 2.10, show that μ_k decreased from 0.29 ± 0.03 to 0.17 ± 0.02 as the deposition temperature was raised from 15 to 450 °C. The coefficient was relatively unchanged after annealing, when uncertainty is taken into account. The scratch tests show that the 450 °C-dep/450 °C-ann film had the best tribological (wear resistance and coefficient of friction) properties in this study.

In summary, the effect of synthesis temperature on the composition and structure, and optical, electrical, and mechanical properties of reactively-sputtered titanium oxide thin films has been systematically investigated. Raising the deposition temperature did not result in a crystalline TiO_2 sample, but instead reduced x in TiO_x. This was attributed to decreased target poisoning during the reactive sputter deposition process. The reduced oxidation resulted in decreased film transmittance and resistivity. Modulus, hardness, and wear resistance were observed to increase with deposition temperature, and this was attributed to film densification. After annealing for 30 mins at 450 °C in air, each film became transparent and insulating, but the mechanical properties remained substantially (50% or more) different. These results show that the coupled effects of deposition temperature and post-deposition annealing can have a competing influence on the properties of titanium oxide thin films.

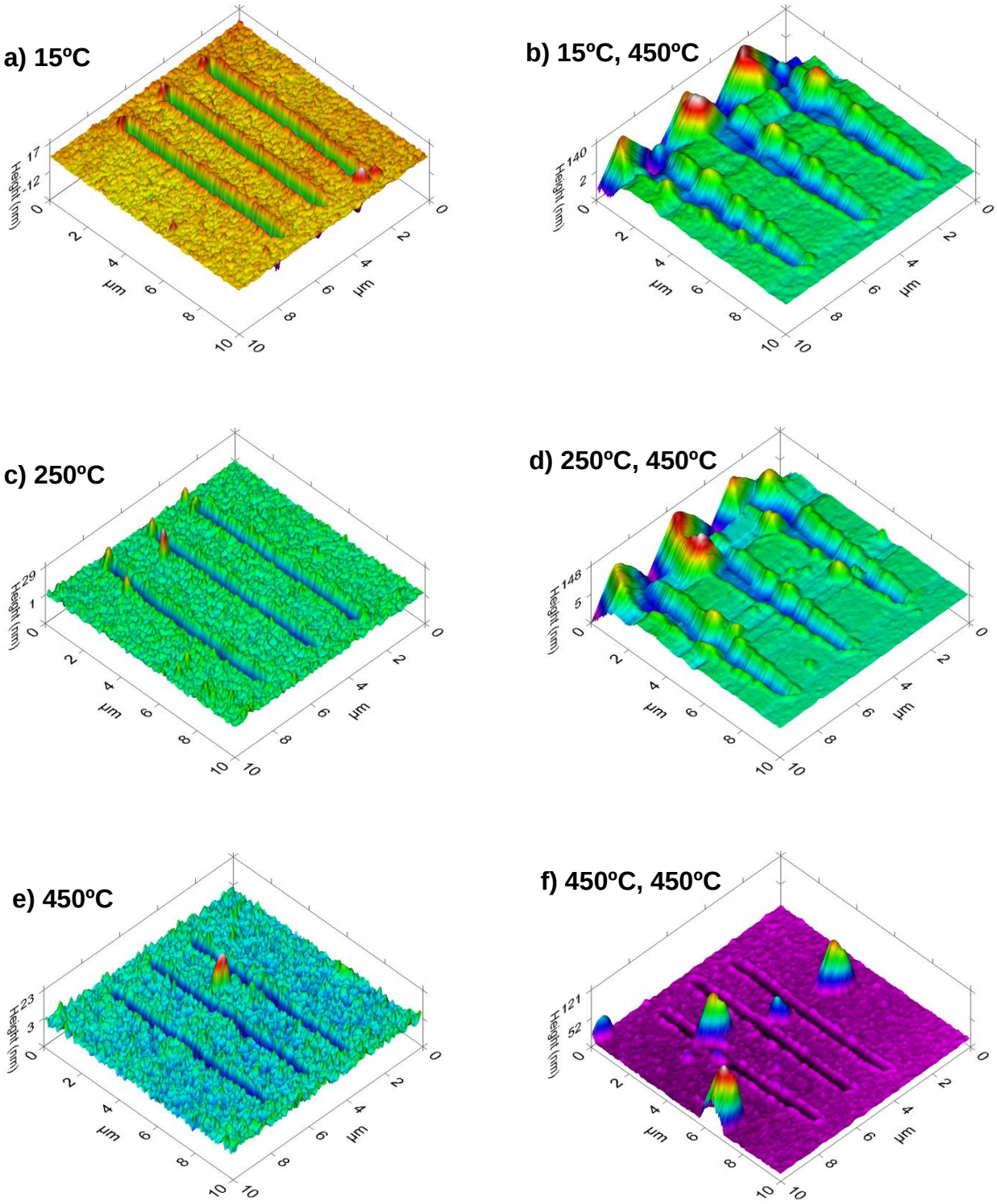

Fig. 2.8. SPM topographies of TiO_x films after nanoscratch tests.

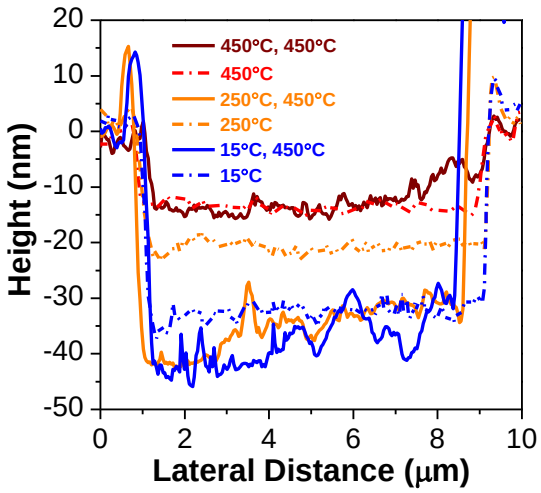

Fig. 2.9. Scratch profiles for constant load of 500 μN with Berkovich tip.

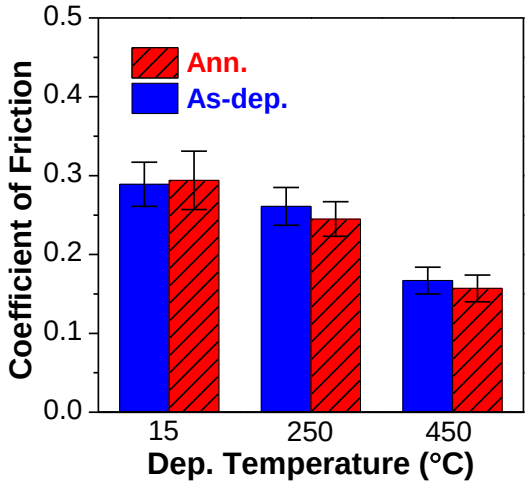

Fig. 2.10. Coefficient of friction for TiO_x films based on nanoscratch tests.

2.5 Conclusions

In this study, the combined effects of deposition temperature and post-deposition annealing on the optical, electrical, mechanical, and tribological properties of titanium oxide thin films were investigated. Based on high-resolution XPS, it was determined that the films became more metallic as the deposition temperature was raised from 15 to 450 °C. Moreover, the mechanical

and tribological properties of the film deposited at 450 °C were at least 50% greater than for the film deposited at 15 °C. This difference was attributed to film densification.

After annealing at 450 °C for 30 mins in air, the films all became transparent and insulating. However, the annealing process had mixed effects on the mechanical and tribological properties such that the 15 and 250 °C films softened, but the 450 °C film hardened. This mixed trend was attributed to the different as-deposited stoichiometries. The results show that the combined effects of deposition temperature and post-deposition annealing are quite complex and that the mechanical properties of TiO_2 thin films can be controlled independently of their optical and electrical properties. By increasing synthesis temperature the material can be strengthened. However, the results also show that post-deposition annealing can have a potentially deleterious effect on the mechanical properties and should therefore be monitored and controlled carefully. This knowledge is important because TiO_2 coatings are often used as the outer-most layers in optical devices.

3 Influence of Na Diffusion on Thermochromism of Vanadium Oxide Films and Suppression through Mixed-alkali Effect

3.1 Overview

Vanadium(IV) oxide possesses a reversible first-order phase transformation near 68 °C. Potential applications of the material include advanced optical devices and thermochromic smart windows. In this study, vanadium oxide films were grown on three types of glass substrates using reactive DC magnetron sputtering and were then annealed in air. The substrates were characterized with energy-dispersive X-ray spectroscopy, and the films were characterized with X-ray photoelectron spectroscopy, X-ray diffraction, scanning electron microscopy, atomic force microscopy, transmission electron microscopy, and UV-Vis-NIR spectrophotometry. The results show that the composition of the substrate has a major impact on the microstructure and optical properties of the deposited films. Sodium (Na) in the glass can undesirably inhibit thermochromism; however replacing half of the Na with potassium (K) suppresses the Na diffusion and promotes the nucleation of pure VO_2 with superior thermochromic functionality. The improved performance is attributed to the mixed-alkali effect between Na and K. These findings are both scientifically and technologically important since soda (Na_2O) is an essential flux material in glass products such as windows.

3.2 Introduction

Vanadium(IV) oxide possesses a reversible first-order phase transformation near 68 °C [11]. Below the critical temperature, τ_c, it is semiconducting with a monoclinic structure and above τ_c it converts to a rutile tetragonal structure with metallic characteristics [12]. Optical, electrical, magnetic, and mechanical properties change abruptly at the transition temperature [13, 15-17]. Potential applications of the material include advanced optical devices and thermochromic smart windows [6, 7, 19, 20, 57]. Synthesis of the material commonly requires temperatures exceeding 200 °C [6, 7, 27, 58-62]. In the literature, VO_2 films have typically been deposited on fused quartz (high purity SiO_2), monocrystalline Si, or other substrates that are not favorable for widespread usage of the material [7, 27, 58-61]. Common glass substrates have generally been avoided so as to prevent the diffusion of sodium into the vanadium oxide films, and when this diffusion has been observed it was neither investigated in detail nor was a solution proposed for its suppression [63]. In some cases a diffusion barrier layer has been deposited on the substrate prior to the VO_2 layer [27], but again this restriction is not ideal for many applications. For practical usage of the material in the thin film form, inexpensive, visibly-transparent and thermally-stable substrates are needed.

In this work it is shown that synthesis temperatures exceeding 200 °C are sufficient to activate the diffusion of sodium (Na) from common soda-lime glass substrates into vanadium oxide films. The resulting $Na_xV_2O_5$ material lacks the thermochromic properties that make VO_2 attractive for smart windows and other applications. However, Na diffusion is suppressed by replacing half of the Na with potassium (K) and taking advantage of the mixed-alkali effect between these ions. The VO_2 film grown on this type of glass has the desired thermochromism, and its properties match or exceed those of the control sample on fused quartz. This finding is

scientifically and technologically important because soda (Na_2O) is an essential flux material in common glass products such as windows.

3.3 Experimental Procedure

Three types of glass were selected for growing vanadium oxide films: (1) silica-soda-lime (SL), (2) silica-potash-soda (PS) and (3) fused quartz (FQ). The thicknesses of the SL, PS and FQ substrates were 1.0 mm, 0.5 mm and 1.5 mm, respectively. The compositions of these materials were obtained using an FEI Sirion scanning electron microscope (SEM) equipped with energy-dispersive X-ray spectroscopy (EDS). Thin vanadium oxide films were deposited on the substrates by reactively sputtering a 99.9% pure vanadium target (50.8 mm diameter × 6.35 mm thickness) in a mixed Ar + O_2 environment using an Orion 5 UHV magnetron sputtering system (AJA International, Inc.). The films were deposited while maintaining a substrate temperature of 200 ± 5 °C using a PID controller with feedback from a Type K thermocouple. The deposition power was controlled at 100 W and the distance between target and substrate was approximately 130 mm. Ar and O_2 flow rates were 19 and 1 sccm, respectively, and absolute deposition pressure was 0.47 Pa. These conditions resulted in a calibrated deposition rate of 4.7 nm/min. The deposition process was controlled carefully since the structure and properties of reactively-sputtered thin films are known to rely strongly on the processing conditions [64-66]. Following the deposition, samples were annealed in quiescent air at 365 °C for 30, 60 and 90 mins, respectively, using a Barnstead Thermolyne 47900 furnace.

The thickness of the films was measured using the scanning probe microscopy (SPM) function of a Ubi1 nanomechanical test instrument (Hysitron, Inc.). The compositions of the as-deposited and 90 min annealed samples were characterized with X-ray photoelectron

spectroscopy (XPS) using a Surface Science Instruments S-Probe. Monochromatic Al K_α was used as the radiation source for XPS, and the data was analyzed with CasaXPS 2.3.15. The spectra were corrected such that the C 1s binding energy was 284.6 eV, which is a standard practice for XPS analysis [67, 68]. Three spots per sample were characterized to allow for basic statistical analysis.

Microstructures of the samples were characterized with X-ray diffraction (XRD) using a Bruker D8 Discover with GADDS. Cu K_α was used as the radiation source for XRD, and data was collected from 2θ of 15 to 70°. Naturally-fractured cross sections and surfaces of the as-deposited and annealed samples were characterized with an FEI Sirion scanning electron microscope (SEM) in secondary electron detection mode. This technique provided details about microstructure and also served as a means to verify the thickness of the films. Surface morphologies were also characterized with a Veeco Dimension Icon-PT atomic force microscope (AFM) in acoustic AC mode (equivalent to tapping mode). The scan area was 1×1 μm^2, and the data was analyzed with Bruker NanoScope Analysis 1.5. The microstructures of the samples were further probed using transmission electron microscopy (TEM) with an FEI Tecnai G2 F20. The instrument was also used to perform selected area electron diffraction (SAED). Optical transmittance was obtained with UV-Vis-NIR spectrophotometry using a Varian Cary 5000. The measurement was performed between wavelengths of 250 and 2500 nm at sample temperatures of 25 and 85 °C, respectively. Heat was supplied with a Peltier heat pump and the system was controlled using a PID controller with a type K thermocouple in contact with the sample. The characterization techniques used in this study provided the ability to detect impurities and determine their effects on the properties of the vanadium oxide films.

3.4 Results and Discussion

Prior to depositing the vanadium oxide films, the compositions of the three types of substrates were analyzed using EDS. The results, provided in Table 3.1, show that the two common glass substrates (SL and PS) comprised a variety of oxides while the FQ substrate consisted of high purity SiO_2. The primary constituents after SiO_2 were Na_2O and CaO for SL glass and K_2O and Na_2O for PS glass. In the following paragraphs, the diffusion of Na^+ ion into the films will be emphasized because this impurity was detected in the top 5 nm of the 200 nm thick film on SL glass and it was found to have a strong impact on the structure and properties of the material. The atomic percentage of Na was 9.5, 4.2, and 0.0%, respectively, for the three different glass substrates.

Table 3.1. Compositions of uncoated glass substrates from EDS analysis. SL, PS, and FQ denote soda-lime, potash-soda, and fused quartz, respectively.

	SL	PS	FQ
	At.%	At.%	At.%
O	59.2	60.6	66.9
Si	25.6	23.6	33.1
Na	9.5	4.2	-
Ca	2.4	-	-
Mg	2.2	-	-
K	0.5	5.2	-
Al	0.5	1.9	-
S	0.1	-	-
Zn	-	2.9	-
Ti	-	1.4	-
Sb	-	0.3	-

After the EDS analysis of the substrates, vanadium oxide films of up to 200 nm thickness were then deposited under the conditions described in Section 2, and the film composition was analyzed using XPS.

Fig. 3.1 shows the XPS spectra for the 200 nm thick as-deposited and 90 min annealed films synthesized on all three substrates. Besides the expected V and O elements, the films on PS glass and FQ possessed nearly zero impurities, except for carbonaceous contamination possibly from the vacuum pump oil, and a negligible amount of Si on PS. However, a notable Na 1s peak was detected for the sample on SL glass indicating Na diffusion from the SL substrate throughout the entire 200 nm thickness of the film. A detailed view of this region is shown in Fig. 3.2(a) and the normalized Na atomic percentages are shown in Fig. 3.2(b). From XPS it was determined that the atomic percentage of Na in the top 5 nm (approximate characterization depth of XPS) of the as-deposited films on SL was already 2.6%. This shows that the 200 °C deposition temperature was clearly sufficient to activate the diffusion of Na into the film. For the films grown on PS glass and fused quartz, the atomic percentage of Na was below the detection limit of 0.1 to 0.5 at.%. After annealing for 90 mins at 365 °C, the Na content in the top 5 nm of the 200 nm thick film on SL glass increased to 7.5 at.%. This is a large fraction considering that the substrate itself only consisted of 9.5 at.% Na. By contrast, the films grown on PS glass showed almost no Na content before or after annealing.

With the aim to gain more insights on Na diffusion along the film thickness direction, additional films with thicknesses of 25, 50, 100, 150 and 200 nm were synthesized and then characterized with XPS. It was assumed that the compositions of the thinner films were representative of the 200 nm film at the same depth; i.e. the composition of the 100 nm film was similar to the composition of the 200 nm film at half of its thickness. This assumption is justified

because the films are much thinner (0.1%) than the substrates on which they are grown, and the substrates serve as potential sources of impurities; i.e. sodium diffusion. Thus there is a sufficient availability of impurities from the substrate that the composition at the interface can be considered constant (Dirichlet boundary condition). This approach enabled a sodium concentration profile to be determined for the as-deposited and 90 min annealed samples, as shown in Fig. 3.3. Note that FQ samples are excluded since Na was not detected in any of those films. The Na content of the as-deposited films on SL glass ranged from 2.5 to 8.5% in a nearly exponential distribution. After annealing, the Na content of the SL samples was greater than 7 at.% for each film thickness characterized; 25, 50, 100, 150 and 200 nm. For the films on PS glass, no Na was detected in the as-deposited samples. After annealing for 90 mins, only the 25 and 50 nm thick films showed measurable Na content at 4.0 and 2.4 at.%, respectively. Therefore Na diffusion did occur for this substrate, but at a rate many orders of magnitude slower than that of the SL glass. The difference between the Na diffusivities of the SL and PS samples may be attributed to two reasons. First, the PS glass had a lower percentage of Na, which resulted in a smaller concentration gradient and driving force for diffusion. Second and more importantly, the PS glass comprised K_2O which led to a mixed-alkali effect with Na_2O. It has been reported in literature that the mixed-alkali effect changes alkali diffusivity in a non-linear fashion [69, 70].

The microstructures of the 200 nm thick as-deposited and annealed films were characterized with XRD and the results are presented in Fig. 3.4. The as-deposited films on all three substrates are shown to be amorphous, but measurable crystallinity was detected for all films after annealing. However, the composition and structure were different for the films on SL glass compared to those on PS glass and FQ. The film deposited on SL glass developed an orthorhombic $Na_xV_2O_5$ structure (space group $P2_1mn$; No. 31) after annealing, as shown in Fig.

3.4(a). The films on PS glass and FQ crystallized into the desired monoclinic VO_2 structure (space group $P2_1/c$; No. 14) with dominant peaks of (011) and $(\bar{2}11)$ as shown in Fig. 3.4(b) and (c). The preferred orientation of all the VO_2 samples was (011), except for the 30 min annealed sample on PS glass which had a preferred orientation of $(\bar{2}11)$. The symbols in Fig. 3.4 correspond to reference data from the International Center for Diffraction Data [25, 71]. The XRD results show that sodium diffusion from SL glass can lead to the formation of a different microstructure compared to PS glass and FQ which do not have this effect.

The compositional results from EDS and XPS analyses, as well as the crystallinity information from XRD enabled the development of an equation which could be used to describe the Na diffusion process. The data show that the sodium silicate chains in the SL glass decomposed somewhat as the synthesis temperatures (deposition and annealing) exceeded 200 °C. This may have occurred because the ionic bond that holds Na to the silicate chains is relatively weak, and in turn the Na ionic mobility increases significantly with temperature. Furthermore, the vanadium oxide structure of the film is relatively open and readily accommodates the diffusion of the Na^+ ion. The incorporation of this impurity induced an orthorhombic $Na_xV_2O_5$ structure for the film on SL glass. Here: $0.19 \leq x \leq 0.57$, which was calculated from the XPS results shown in Fig. 3.2(b). The equation that theoretically describes the nucleation of $Na_xV_2O_5$ can be written as:

$$2Na_2O + 4VO_2 + O_2 \rightarrow 2Na_{2-x}O + 2Na_xV_2O_5 \qquad (3.1)$$

The left-hand side (LHS) corresponds to the condition where adatoms of vanadium oxide have been adsorbed to the SL substrate, but Na has not yet had time to diffuse into the film. The right-hand side (RHS) corresponds to the as-deposited and annealed films. The compositions were directly calculated by XPS for the RHS, while the adatom composition of the LHS was inferred

based on the monoclinic VO_2 films synthesized on PS glass and FQ (which were produced at the same time). The cause of the conversion from VO_2 adatoms to the $Na_xV_2O_5$ film appears to be the incorporation of the Na^+ ion from the SL glass. This diffusion continues until the concentration gradient of Na equilibrates ($x \rightarrow 0.735$ as Na content $\rightarrow$ 9.5 at.% which corresponds to the composition of the SL substrate) and the driving force vanishes.

To further confirm the above postulations, the change in Gibbs free energy was calculated to check that the diffusion process is consistent with the laws of thermodynamics. For this purpose, the chemical reaction can be expressed as:

$$2Na_2O + 4VO_2 + O_2 \rightarrow 4NaVO_3 \tag{3.2}$$

The product of Eqn. (3.2) was written as $NaVO_3$ to simplify the thermodynamic calculations. It corresponds to the theoretical case of full conversion of reactants to sodium vanadate. The standard free-energy change (ΔG°) is calculated as:

$$\Delta G^\circ = \Delta H^\circ - T\Delta S^\circ \tag{3.3}$$

where ΔH° is the change in standard enthalpy, T is the annealing temperature (638 K), and ΔS° is the change in standard entropy. The standard free-energy change for the reaction (ΔG°_{rxn}) is fully expressed as:

$$\Delta G^\circ_{rxn} = \Big\{\big\{4\Delta H^\circ_f(NaVO_3) - \big[2\Delta H^\circ_f(Na_2O) + 4\Delta H^\circ_f(VO_2) + \Delta H^\circ_f(O_2)\big]\big\} - T\{4S^\circ(NaVO_3) - [2S^\circ(Na_2O) + 4S^\circ(VO_2) + S^\circ(O_2)]\}\Big\} \tag{3.4}$$

The values of the standard enthalpy of formation (ΔH°_f) and standard entropy (S°) were obtained from *NBS (NIST) Tables of Chemical Thermodynamic Properties* [72]. The resulting ΔG°_{rxn} is calculated to be $-833\ \mathrm{kJ \cdot mol^{-1}}$. The negative value of ΔG°_{rxn} indicates that this chemical reaction is spontaneous process in the forward direction at 365 °C. In other words, the

diffusion of Na observed in this work is consistent with the 2nd Law of Thermodynamics because it results in an increase in the entropy of the universe and a reduction in Gibbs free energy.

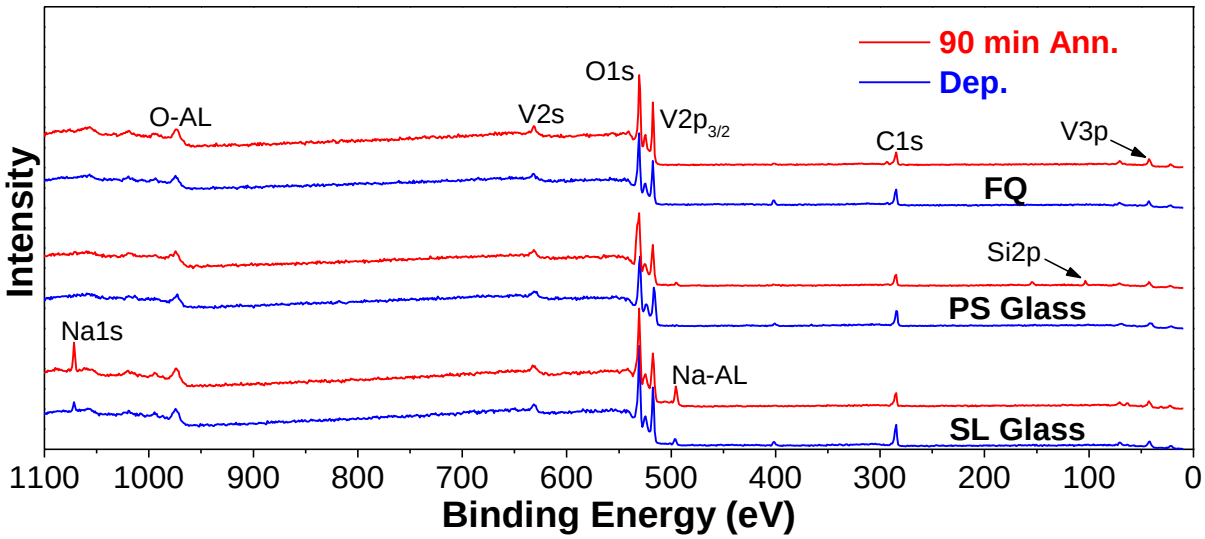

Fig. 3.1. XPS survey spectra for the 200 nm thick as-deposited and 90 min annealed vanadium oxide films on the three different substrates. The "-AL" denotes an Auger Line, which was not used for this analysis.

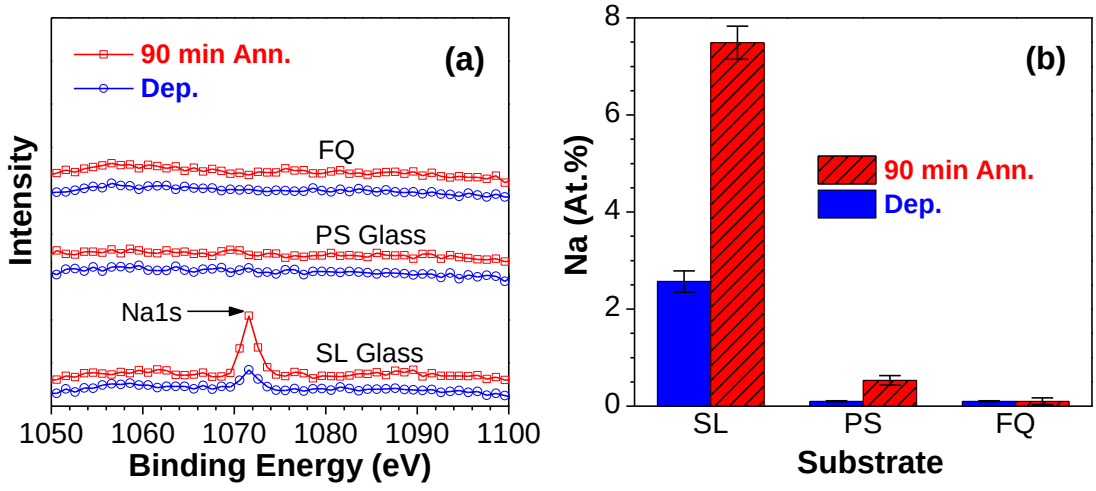

Fig. 3.2. (a) Na1s region of XPS data for the as-deposited and 90 min annealed films on the three different substrates. (b) Atomic percentage of Na in the top 5 nm of the films based on XPS analysis.

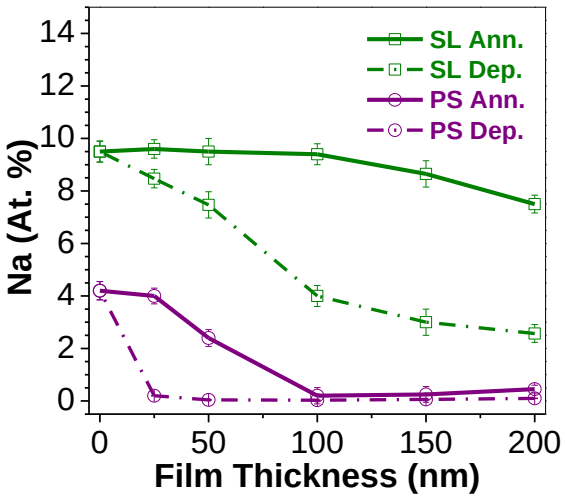

Fig. 3.3. Sodium concentration as a function of film thickness for the as-deposited and 90 min annealed films on SL and PS glasses. The “0” thickness corresponds to the uncoated substrate.

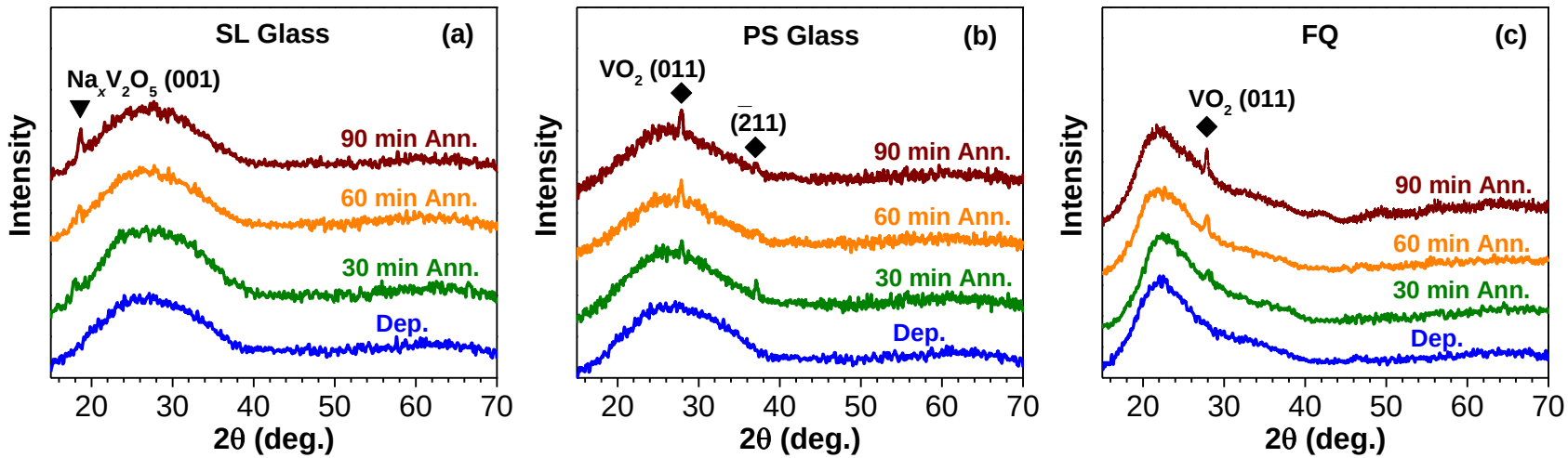

Fig. 3.4. XRD spectra for the 200 nm thick as-deposited, and 30, 60, 90 min annealed films on: (a) SL glass showing clear $Na_xV_2O_5$ peaks after annealing, (b) PS glass showing VO_2 (011) and $(\bar{2}11)$ peaks after annealing, and (c) FQ showing clear VO_2 (011) peaks after annealing. Symbols correspond to reference data from ICDD [25, 71].

Since grain size and shape can have an important influence on the properties of vanadium oxide thin films, this information was obtained using a scanning electron microscope. Naturally-fractured cross sections of the 200 nm thick as-deposited and 90 min annealed films are shown in Fig. 3.5, and surface morphologies for the 200 nm thick as-deposited, and 30, 60, 90 min annealed films are shown in Fig. 3.6. The cross-sectional images verify that the thicknesses of the films are each 200 ± 10 nm. The images also show that the as deposited films are smooth and composed of nanoscale clusters. However, after annealing, the microstructure of the films became much coarser, particularly for the films on SL glass. The surface SEM images show more detailed microstructural evolution of the films from deposition to after annealing. For films on all three substrates, the fine clusters in the as-deposited films evolved into increasingly larger and rougher grains after annealing. For the films on SL glass, the grains appeared as nanomesas. The film on PS glass comprised spheroidal grains up to 60 mins of annealing, at which time nanorods grew from the base coating. The FQ sample had generally flat grains which coarsened after 60 mins and then partially coalesced at 90 mins. The SEM results in this work show that the substrate composition has profound effect on the morphology of the sputtered films and that a visibly coarser and rougher morphology is produced for the film grown on SL glass.

The surface morphologies of the films were probed further through atomic force microscopy. The AFM results correspond well with the SEM characterizations. Topographies and root-mean-square roughness (R_q) values of the 200 nm thick as-deposited and 90 min annealed films are shown in Fig. 3.7. R_q values were calculated from the 1×1 μm^2 areas shown in the figure. The rms roughness of each sample is quite small, ranging between 1.7 and 4.3 nm; except for the annealed film on SL glass which had a much larger roughness of 21 nm. The topography is different from sample to sample, especially for the annealed cases. Compared to the PS and FQ

samples, the film on SL glass showed much rougher structures with peak-to-valley depth of over 150 nm. In terms of feature size, the 90 min annealed films on PS glass and FQ had grains on the order of 50 nm, but the film on SL glass was much coarser with grains on the order of 150 to 200 nm. This data quantitatively shows that the films on SL glass had a dramatically different morphology than those on PS glass and FQ. The XPS and XRD results shown in Fig.3.1 - 4 elucidate that the rougher morphology is associated with the diffusion of sodium into the film and the formation of $Na_xV_2O_5$ ($x \approx 0.57$ for the 90 min annealed sample).

It was also desired to know how the diffusion of Na into the vanadium oxide films affected the local crystallinity and microstructure. To gain this information, sample cross sections with 40 nm in-plane (transverse) thickness were prepared using the focused ion beam (FIB) of an FEI XL 830 Dual Beam FIB/SEM and then characterized with an FEI Tecnai TEM. Details of the sample preparation process can be found elsewhere [73]. TEM images of the cross sections are shown in Fig. 3.8(a) and (b). The results show that the interface between the $Na_xV_2O_5$ film and the SL glass was more diffuse and less clear than the interface between the VO_2 film and the PS glass. Also, clearer lattice fringes and crystallinity were detected for the VO_2 film compared to the $Na_xV_2O_5$ film. The formation of noticeable dark spots or nanoclusters can be seen in Fig. 3.8(a) which was apparently associated with the diffusion of sodium into the vanadium oxide film. HRTEM images of the samples are provided in Fig. 3.8(c) and (d). These images reinforce the observation that higher quality crystallinity was obtained for the VO_2 on PS glass compared to the $Na_xV_2O_5$ on SL glass. The film on SL glass comprised both crystalline and amorphous content with a relatively rough microstructure, whereas the film on PS glass had a very regular and periodic microstructure corresponding to monoclinic VO_2. The $Na_xV_2O_5$ on SL glass was too disordered to establish the orientation of the grains shown in Fig. 3.8(c), but the VO_2 on PS glass

was sufficiently periodic for its orientation to be determined. The $[011]$ and $[\bar{2}11]$ directions of the grain are indicated in Fig. 3.8(d). The drastic difference between the microstructures of the samples was due to the Na diffusion detected with XPS and reported in Fig. 3.3. Crystallinity of the samples was originally determined with XRD and was later verified using selected area electron diffraction (SAED). Representative SAED patterns are shown in Fig. 3.8(e) and (f). Less intense coherent diffraction was detected for the sample on SL glass due to its higher amorphous content. For the VO_2 film on PS glass, some distinct spots were observed in the SAED pattern because the size of the grain characterized was on the order of 100 nm. Therefore the diffraction pattern had intermediate characteristics between mono- and poly-crystalline samples which produce spots and rings, respectively. Lattice spacings of the samples were identified and confirmed using reference files from the International Center for Diffraction Data [25, 71]. Only the (001) plane could be clearly identified for the $Na_xV_2O_5$ on SL glass, however several planes could be identified for the VO_2 on PS glass. Two important indices, (011) and $(\bar{2}11)$, are annotated in Fig. 3.8(f) for reference. These results confirm that PS glass is a much more suitable substrate than SL glass for producing high quality VO_2 films.

In the literature VO_2 morphologies with grains varying in shape from spheroidal to worm-like have been reported with dimensions on the order of 10 to 1000 nm [27, 60, 61]. A brief discussion of these studies is provided in the following sentences. H. Cui et al. used reactive DC magnetron sputtering to deposit VO_2 films that had bar-shaped grains with dimensions from 60 to 140 nm [74]. H. Zhang et al. reactively DC sputtered VO_2 films with round to polygonal grains on the order of 40 to 100 nm [75]. M.J. Miller and J. Wang (the authors of the current study) reactively DC sputtered VO_2 films with needle-like grains that coarsened from 30 to 70 nm as annealing time increased from 30 to 75 mins [18]. M. Gurvitch et al. RF sputtered pure V

films and then oxidized them in O_2. This technique, which they referred to as the "precursor oxidation process," resulted in films comprising round grains varying in diameter from 50 to 200 nm [76]. Melnik et al. reactively DC sputtered VO_2 films with grains on the order of 20 nm based on the full-width half-maximum of the XRD peaks and the Scherrer's equation [62]. Manning et al. used atmospheric pressure chemical vapor deposition to produce VO_2 films with worm-like grains, which was an extreme case of the Volmer-Weber (island) growth mode [27]. In another study, J. Suh et al. used pulsed laser deposition (PLD) to produce round grains that coarsened from 50 to 200 nm as annealing time increased from 5 to 80 mins [61]. Other groups used the sol-gel method to deposit VO_2 films with spheroidal grains from 50 to 200 nm in diameter [60, 77]. Z. Zhang et al. used a solution-based technique to deposit VO_2 on SnO_2:F (FTO) glass substrates [78]. By employing both SEM and TEM characterizations, the films in that study were shown to have round grains on the order of 100 nm. High quality crystallinity was observed through TEM and SAED characterizations. V. Morrison et al. also utilized TEM and SAED to characterize PLD-grown VO_2 films with polygonal grains on the order of 100 to 400 nm [79]. Taken as a whole, these studies show that the complex growth kinetics of VO_2 result in myriad morphologies, textures, and grain sizes. The common unifying aspect in each work is the monoclinic lattice of the semiconducting form and the rutile tetragonal lattice of the metallic form of vanadium(IV) oxide.

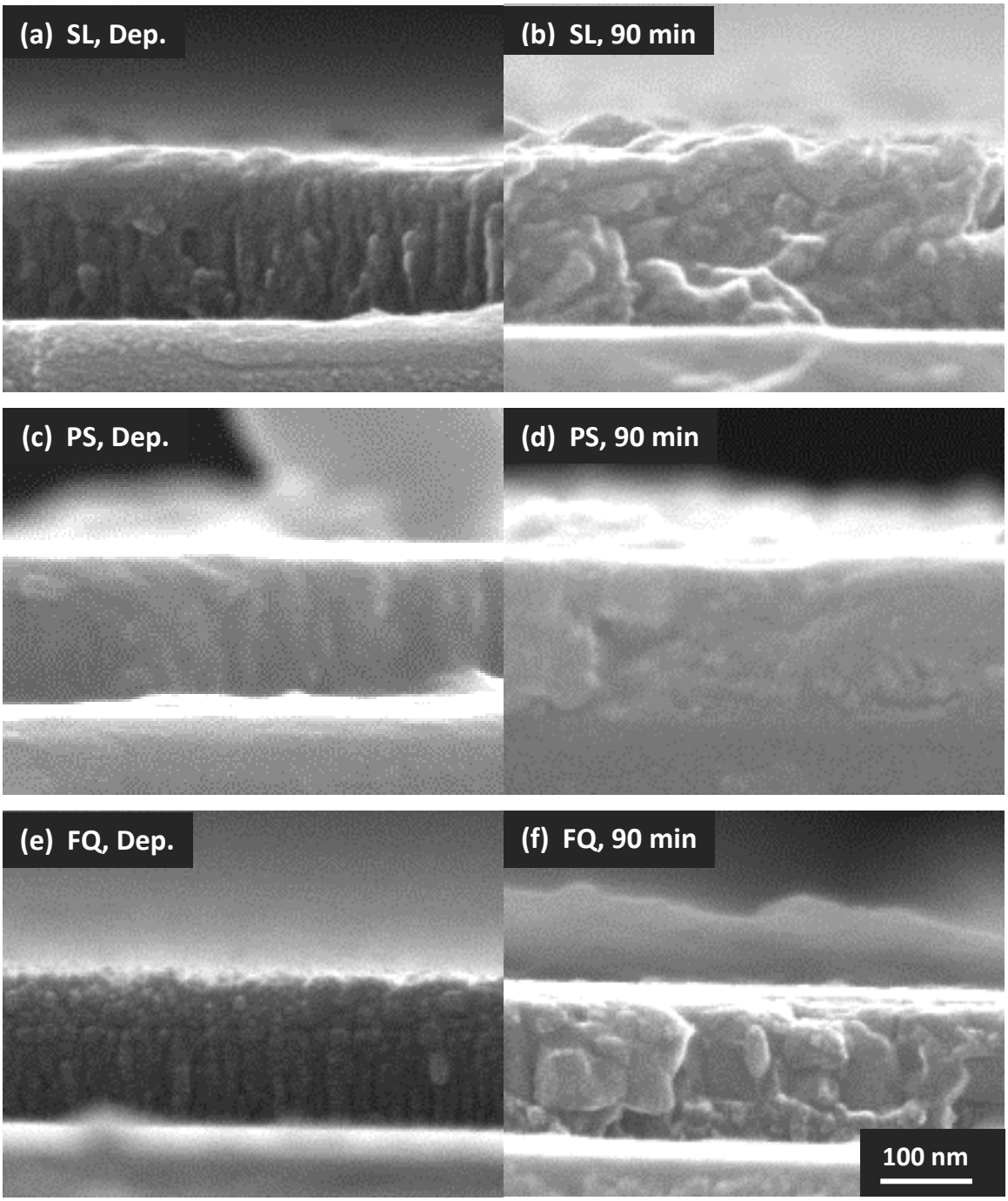

Fig. 3.5. Cross sectional SEM images of both as-deposited and 90 min annealed films on (a-b) SL glass, (c-d) PS glass, and (e-f) FQ. The scale bar applies equally to each image. The thickness of each film is confirmed to be 200 ± 10 nm.

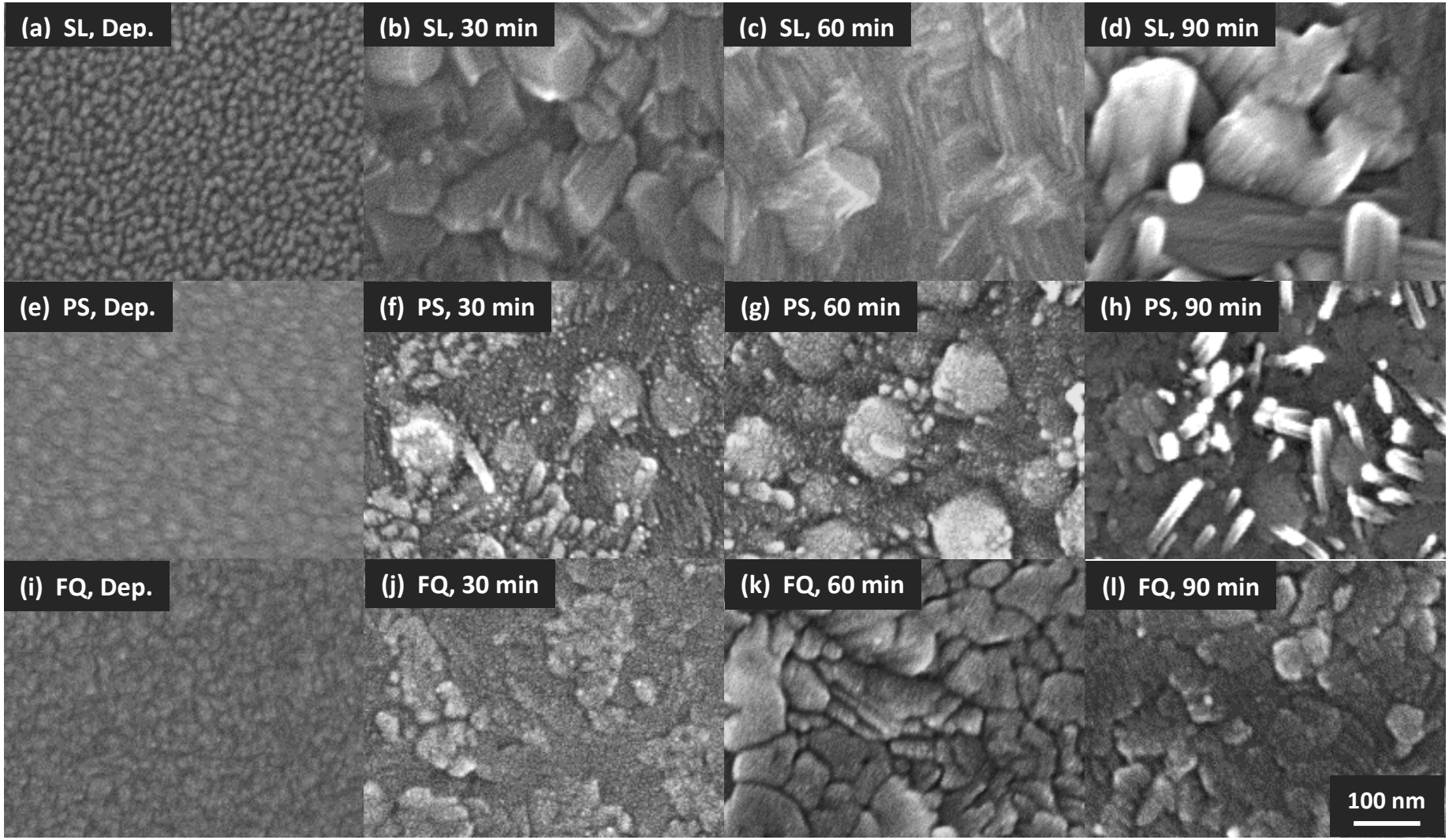

Fig. 3.6. Surface morphologies of the 200 nm thick as-deposited, and 30, 60, 90 min annealed films on (a-d) SL glass, (e-h) PS glass, and (i-l) FQ.

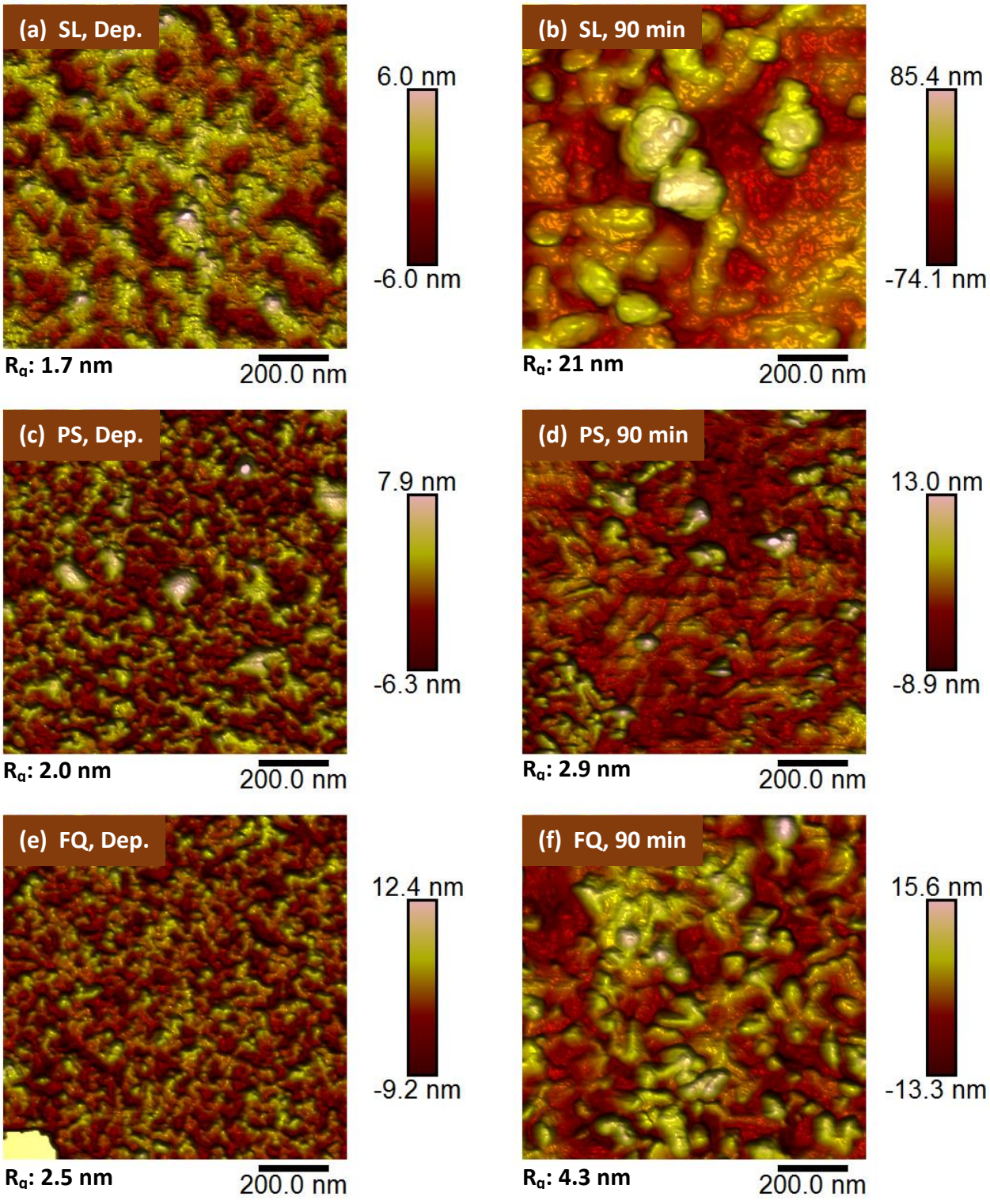

Fig. 3.7. Surface topographies of the 200 nm thick as-deposited and 90 min annealed films on (a-b) SL glass, (c-d) PS glass, and (e-f) FQ, obtained with AFM in acoustic AC mode (equivalent to tapping mode). The scan area was 1×1 μm^2. Root-mean-squared (Rq) surface roughness is provided in the lower left-hand corner of each image.

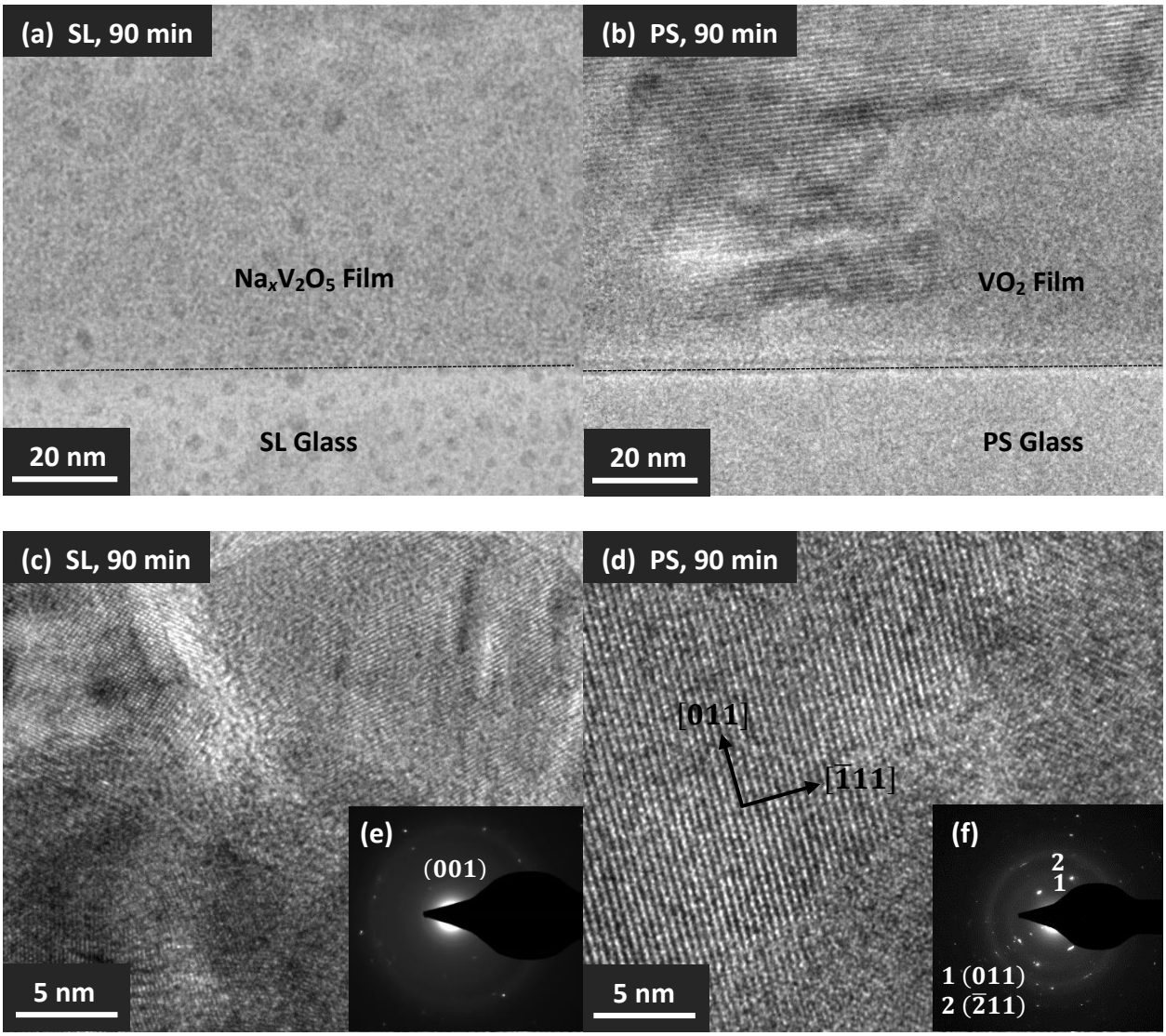

Fig. 3.8. (a) TEM, (c) HRTEM and (e) SAED pattern for orthorhombic $Na_xV_2O_5$ film on SL glass. (b) TEM, (d) HRTEM and (f) SAED pattern for monoclinic VO_2 on PS glass.

The impact of the composition and structure on the optical properties was very clear from the UV-Vis-NIR spectrophotometry measurements. The transmittance spectra presented in Fig. 3.9(a) show that neither the as-deposited (amorphous) nor the annealed ($Na_xV_2O_5$) films on SL glass show significant thermochromism; the transmittance of the samples did not decrease substantially when the temperature was raised from 25 to 85 °C. By contrast the transmittance of the annealed VO_2 films on PS glass and FQ displayed the characteristic thermochromism, as

shown in Fig. 3.9(b) and (c). Also, the absorption edge of the films shifted from approximately 370 nm before annealing to 470 nm after annealing, which resulted in a permanent color change from gray to light bronze. All annealed films on PS glass and FQ showed a significant amount of thermochromic functionality. The films on PS glass had the best overall performance in terms of luminous transmittance and IR modulation.

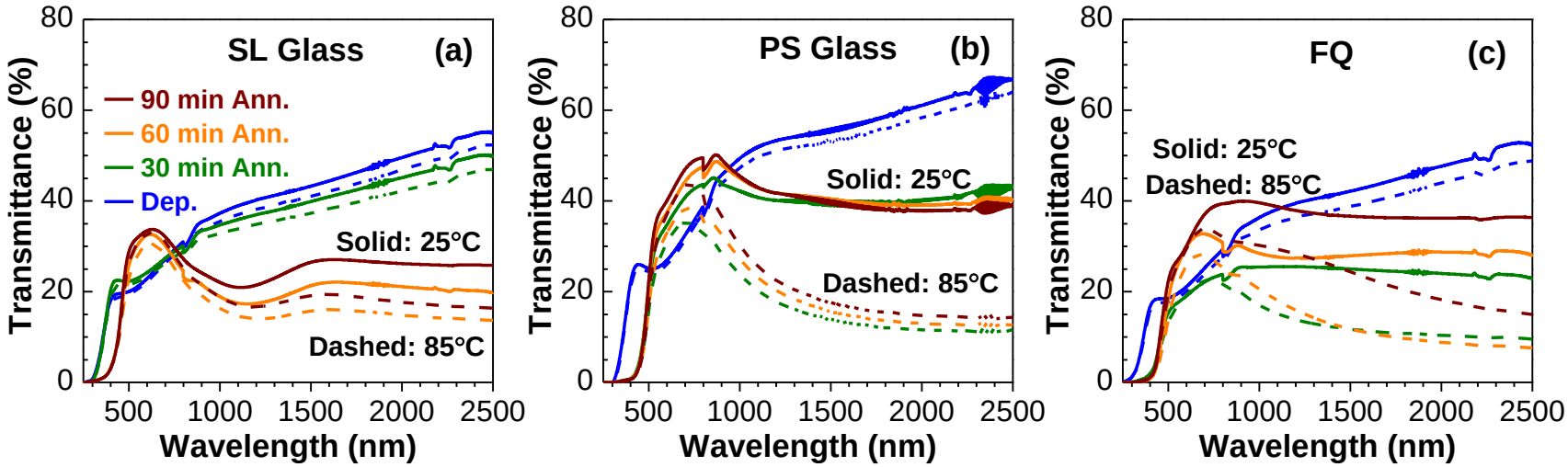

Fig. 3.9. UV-Vis-NIR spectra for 200 nm thick as-deposited (blue), 30 min annealed (green), 60 min annealed (orange), and 90 min annealed (purple) films on: (a) SL glass, (b) PS glass and (c) FQ, measured at 25 ºC (solid lines) and 85 ºC (dashed lines), respectively.

For thermochromic applications, it is highly desirable to know the critical transition temperatures, τ_c, of the samples. Therefore transmittance of the thermochromic VO_2 films on PS glass was measured at a fixed wavelength of 2500 nm while the temperature was cycled between 25 and 85 °C in 2 °C increments. The derivative of the transmittance with respect to temperature was calculated, and the point corresponding to the greatest magnitude of the derivative was defined as τ_c. Representative results for the 200 nm thick 90 min annealed film on PS glass are shown in Fig. 3.10. This characterization elucidates that the average (between cooling and heating) τ_c was approximately 55 °C for the samples in this study. In the literature it has been reported that τ_c for bulk monocrystalline VO_2 is 67 to 68 °C, but it is also known that factors such as grain size, residual stress, percent crystallinity and impurities can affect the transition temperature substantially [7, 18, 61]. In the present study, the relatively low τ_c is attributed to the nanocrystalline structure.

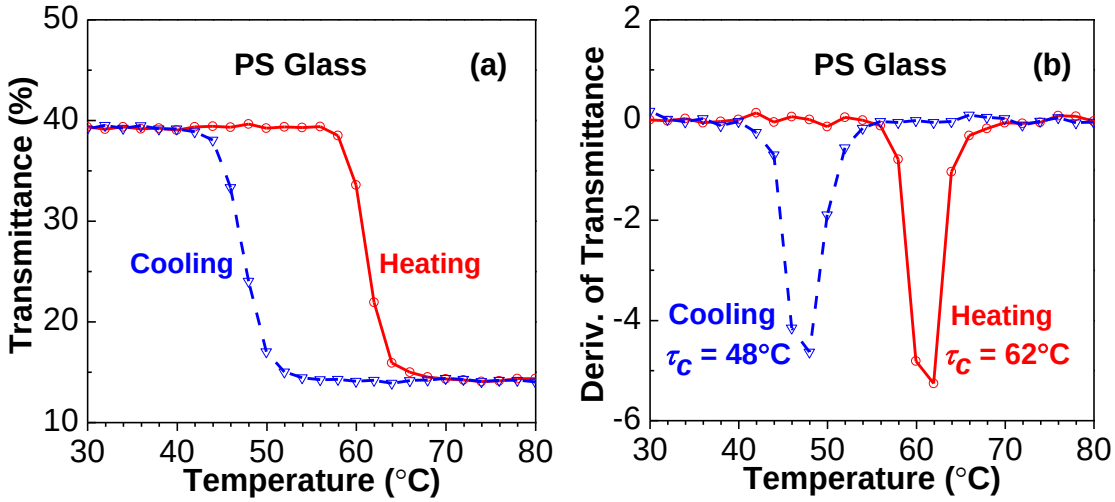

Fig. 3.10. (a) Transmittance of 200 nm thick, 90 min annealed VO_2 film on PS glass at a fixed wavelength of 2500 nm. (b) Derivative of transmittance loop with respect to temperature. The value at the maximum magnitude of the derivative is defined as the critical transition temperature, τ_c.

In summary, stable VO_2 films with strong thermochromic properties were obtained on both PS glass and fused quartz after annealing. This is in contrast to the SL glass, which exhibited excessive Na diffusion and never yielded thermochromic films after annealing. The improved thermal stability of the PS glass is attributed to the mixed-alkali effect between Na and K ions. In the literature, the physical mechanism which causes the mixed-alkali effect is not well understood; however its existence is established [80, 81]. The results in this study show that by replacing half of the Na_2O with K_2O, the mixed-alkali effect makes the PS glass an excellent substrate for producing high quality thermochromic VO_2 films. These findings are likely applicable for many other thin film materials on glass with synthesis temperatures exceeding 200 °C.

3.5 Conclusions

In this work it was shown that synthesis temperatures exceeding 200 °C are sufficient to activate the diffusion of Na into vanadium oxide films deposited on common soda-lime glass. The resulting $Na_xV_2O_5$ material does not possess the desired thermochromic functionality. However, Na diffusion was suppressed by replacing half of the Na with K and taking advantage of the mixed-alkali effect between these ions. The VO_2 film grown on potash-soda glass had the desired thermochromism, and its properties matched or exceeded those of the control sample on fused quartz (pure SiO_2). The results in this study show that the mixed-alkali effect is very beneficial for producing high quality VO_2 films on glass substrates containing sodium. These findings are both scientifically and technologically important since soda (Na_2O) is an essential flux material in glass products such as windows.

4 Influence of Grain Size on Transition Temperature of Thermochromic VO_2

4.1 Overview

Vanadium(IV) oxide (VO_2) is a unique material that undergoes a reversible phase transformation around 68 °C. The material could potentially be used as an energy-efficient coating for windows since its reflectance in the infrared (IR) increases significantly more than in the visible region. Currently VO_2 is limited by a transition temperature (τ_c) that is too high, luminous transmittance that is too low or both. In this study a transition temperature of 45 °C is achieved for a reactively-sputtered, undoped film by restricting grain size to approximately 30 nm. It is concluded that a higher density of grain boundaries (smaller grain size) provides a greater number of nucleating defects which in turn reduces τ_c. Similarly, a higher density of grain boundaries may reduce the hysteresis width (difference between transition temperatures in heating and cooling). Also in this study a new set of optical performance metrics is proposed in which the solar spectrum is divided into the ultraviolet (UV), visible and near infrared (NIR) regions. This approach is more closely aligned with the goals of limiting UV, allowing luminous and modulating NIR transmission. Using these metrics, the optical properties of the low-τ_c sample were: 2% UV transmittance, 47% luminous transmittance and 23% NIR modulation (decrease from 43 to 33%). This study demonstrates that the grain size of VO_2 should be viewed as an important parameter for controlling the transition temperature of the material.

4.2 Introduction

Vanadium(IV) oxide or VO_2 is a unique material that undergoes a reversible phase transformation around 68 °C [11]. Below the critical temperature, τ_c, it is semiconducting with a monoclinic structure, and above τ_c it converts to a rutile tetragonal structure with metallic characteristics [12]. At the semiconducting-to-metallic transition (SMT), properties such as electrical conductivity, magnetic susceptibility, optical transmittance and mechanical stiffness change abruptly [13-18]. From a fundamental standpoint this is an interesting phase transformation with several details still being actively researched, and from an applications perspective there are numerous technologies that could benefit from such a material [19-24].

Given that its optical properties change significantly and reversibly with temperature, VO_2 is a thermochromic material. Furthermore, its transmittance in the infrared (IR) region decreases substantially more than in the visible region when switched to the high-temperature metallic state. Since τ_c is relatively near room temperature, it is possible that a thin film of VO_2 could be used as a smart window coating [6, 7, 57]. The current technical challenge for this material is achieving a transition temperature near 25 °C while still maintaining adequate luminous transmittance and IR modulation [6, 27]. Doping the material with impurities such as W or Cr has been shown to drastically reduce τ_c; however there is generally a tradeoff such that as τ_c is reduced, luminous transmittance decreases, IR modulation decreases or both decrease [6, 27]. Previous work has indicated that there is a size effect in which the nanoscale form of the material has a lower τ_c than the bulk form [7, 11]. The exact cause of this is not well established, but it appears that a high density of grain boundaries disrupts the V-chains of the metallic form which has the effect of lowering τ_c. A transition temperature near 55 °C for nanocrystalline, undoped VO_2 has been reported by various researchers [7, 82]. In this work, τ_c is lowered to 45 °C by

reactively sputtering a 100 nm-thick film with a grain size of approximately 30 nm. No detrimental effect on luminous transmittance or IR modulation is observed. This result shows that VO_2 grain size should be included in the suite of parameters for modifying the transition temperature of the material. Also in this study a new approach for calculating optical performance is proposed. The new method divides the solar spectrum into the ultraviolet (UV), visible, and near infrared (NIR) regions and then uses the air mass 1.5 and luminous efficiency spectra as weight functions for integration [83, 84]. Details of the calculation are provided in Section 4.3. The new method contributes insight into achieving the smart window goals of limiting UV, allowing luminous and modulating NIR transmittance.

4.3 Experimental Procedure

Thin VO_2 films were deposited on glass by reactively sputtering a 99.9% pure vanadium target in a mixed Ar + O_2 environment using an Orion 5 UHV magnetron sputtering system (AJA International, Inc.). The films were deposited while maintaining a substrate temperature of 200 ± 5 °C using a PID controller with feedback from a Type K thermocouple. The coat time was 20 mins, the power was 100 W and the target diameter was 51 mm. The distance between target and substrate was approximately 130 mm. Ar and O_2 flow rates were 19 and 1 sccm, respectively, and the absolute pressure was 0.47 Pa. The deposition process was controlled carefully since the structure and properties of reactively-sputtered thin films are known to rely strongly on the processing conditions. Following the deposition process, samples were annealed in quiescent air at 365 °C for 15, 30, 45, 60 and 75 mins, respectively using a Barnstead Thermolyne 47900 furnace.

The thickness of the deposited films was measured using the scanning probe microscopy (SPM) function of a Ubi1 nanomechanical test instrument (Hysitron, Inc.). The surface morphologies were characterized with an FEI Sirion scanning electron microscope (SEM) in secondary electron detection mode. The working distance for SEM was 5 mm, the accelerating voltage was 5 kV and the spot size was 3. Chemical compositions of the deposited and 75 min annealed films were determined with high-resolution X-ray photoelectron spectroscopy (XPS) using a Surface Science Instruments S-Probe. Monochromatic Al K_α was used as the radiation source for XPS, and the data was analyzed with CasaXPS 2.3.15. Optical transmittance of the samples was obtained with UV-Vis-NIR spectrophotometry using a Varian Cary 5000. The measurement was performed between 250 and 2500 nm at sample temperatures of 25 and 85 °C, respectively. Heat was supplied with a Peltier heat pump and the system was controlled with a PID controller and K Type thermocouple in contact with the sample. Once the data was collected, luminous transmittance of each sample was calculated using the following equation with the luminous efficiency function, φ_{lum}, from Sharpe [84]

$$T_{lum}(\tau) = \int \varphi_{lum}(\lambda) T(\lambda, \tau) d\lambda \,/\, \int \varphi_{lum}(\lambda) d\lambda \tag{4.1}$$

where λ is the wavelength of the incident light, τ is the sample temperature and T is transmittance. T_{lum} is essentially a weighted average of transmittance with respect to the luminous efficiency of the light-adapted eye. Next, averaged transmittance for solar radiation was calculated using the air mass (AM) 1.5 spectrum [85]. Previous researchers calculated a single solar transmittance value above and below τ_c, and the difference between these two values was taken as the solar modulation [6, 86]. This parameter is useful for quantifying potential energy savings for a thermochromic smart window; however it is also inherently nonspecific with respect to the regions of solar light that are being modulated. Furthermore the solar and

luminous spectra peak at nearly the same wavelengths (between 500 and 550 nm). Therefore if 100% total solar modulation is "achieved," then no luminous transmission occurs and the thermochromic coating does not meet its stated design goal of allowing visible light into the built environment. In this study it is proposed that a more precise approach for calculating optical performance is to use the AM 1.5 spectrum for the UV and NIR regions individually. The corresponding domains of integration are 280 to 400 nm and 700 to 2500 nm, respectively. The domain for visible light is 390 to 830 nm, although effectively it is 400 to 700 nm since φ_{lum} is less than 0.5% outside of this domain [84]. The design goals for the UV, visible and NIR regions are as follows. First, no UV transmittance is ever desired for the window coating since exposure to UV radiation can lead to the development of malignant melanoma in humans [87]. Second, 100% visible or luminous transmittance is desired for daylighting purposes in the built environment. Third, 100% NIR modulation is desired to achieve maximum energy efficiency. The VO_2 films in this study were analyzed using these metrics.

After obtaining the transmittance of the films between 250 and 2500 nm, an additional measurement was performed in which the wavelength was fixed at 2500 nm and the temperature was cycled between 25 and 85 °C in 2 °C increments. This was done so that τ_c could be determined. The wavelength of 2500 nm was chosen because the optical behavior of the phase change is clearly observable at this wavelength. The derivatives of the fixed-wavelength transmittance curves were calculated and the greatest magnitude of the derivative was taken as τ_c. The films in this study were also characterized with X-ray diffraction (XRD) using a Bruker D8 Discover with GADDS. The system utilizes a two-dimensional detector with Cu K_α as the radiation source. Data was collected from 2θ of 23° to 57° with a step size of 0.005°, which is fine enough to detect the phase change from monoclinic to tetragonal [25, 88]. For each sample

XRD scans were performed at 25 °C, and for the thermochromic samples the XRD scan was repeated at a sample temperature of 95 °C. The heater used for this characterization was the Anton Paar DCS 350 Domed Cooling and Heating Stage. After XRD spectra were obtained, crystalline grain size was estimated using the full-width at half-maximum (FWHM) of the monoclinic $(\bar{2}11)$ peak and the Scherrer equation [25, 89]

$$d = \frac{K\lambda}{\beta \cos\theta} \tag{4.2}$$

where d is the grain size, K is a dimensionless shape factor assumed to be 0.9, λ is the wavelength of the radiation source (0.154184 nm), β is the FWHM (in radians) and θ is the Bragg angle. The FWHM was measured using the built-in functions of the DIFFRAC.EVA 3.0 software. β was reduced by 0.00232 rad (0.133°) to account for the instrumental contribution to the measured FWHM. This value was estimated based on an LaB_6 standard [90]. The characterization techniques used in this study provided the ability to draw correlations between the grain sizes and transition temperatures of the samples.

4.4 Results and Discussion

The thickness of the films was obtained with a Ubi1 nanomechanical test instrument following the annealing process. High film uniformity was achieved with the sputter deposition process and the resulting thickness was 100 ± 5 nm for each sample in this study. Note that the film thickness in practical smart window applications typically ranges from 25 to 100 nm. This design achieves the highest combination of luminous transmittance and IR modulation [6, 7]. Surface morphologies were characterized with SEM and representative micrographs are provided in Fig. 4.1. The figure shows that the as-deposited and 15 min annealed samples generally lacked

crystallinity. After 30 mins of annealing a more clearly defined spheroidal microstructure began to emerge, and after 45 mins a rod-like crystalline structure was obtained with dimensions on the order of ⌀ 30 × 80 (length) nm. The structures coarsened to roughly 40 × 100 nm after the annealing time reached 75 mins. In the literature, VO_2 grains varying in shape from spheroidal to worm-like have been reported with grain dimensions from 10 to 1000 nm [27].

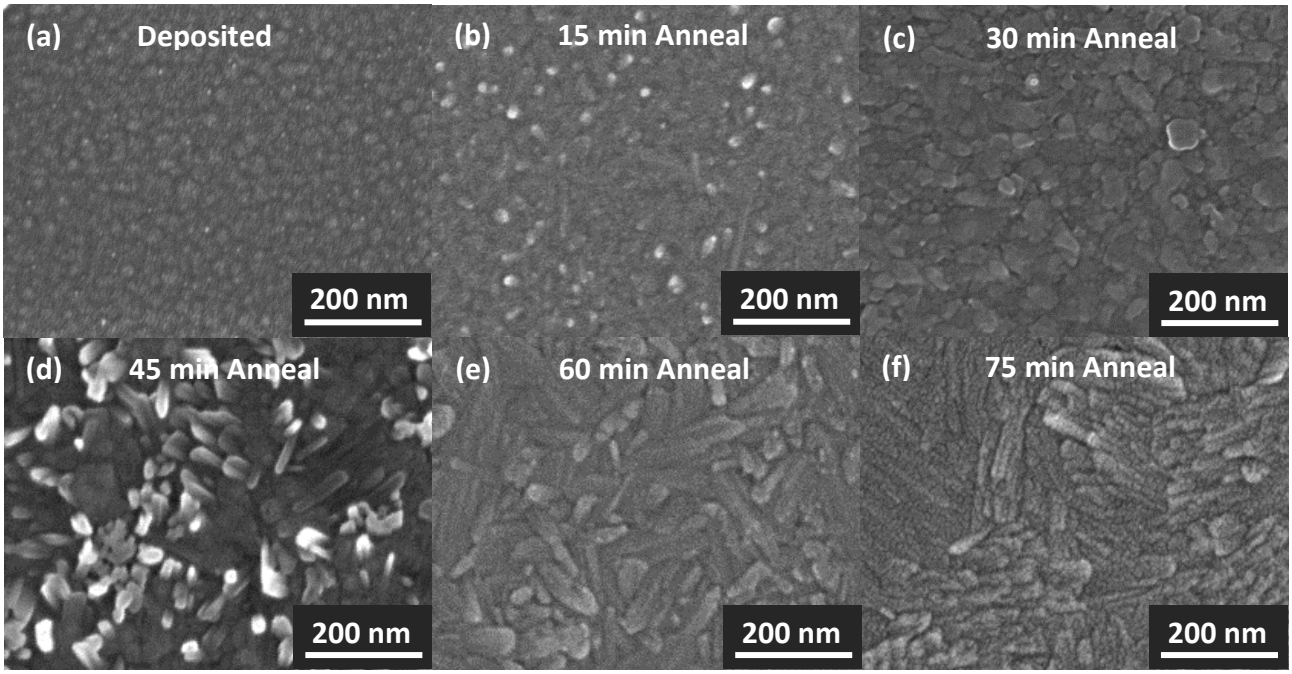

Fig. 4.1. SEM images of VO_2 films: (a) as deposited and (b-f) annealed for 15, 30, 45, 60 and 75 mins, respectively. Average grain dimensions for the samples are approximately: (c) ⌀ 30 nm, (d) 30 × 80 nm, (e) 35 × 90 nm and (f) 40 × 100 nm.

In addition to surface morphologies, chemical composition data was desired to ensure that the samples comprised primarily VO_2 and that they were not excessively oxidized after annealing. High-resolution XPS was performed to gain this information and the results are provided in Fig. 4.2. The results show that approximately 76% of the vanadium in the as-deposited surface (top 10 nm) existed as V^{4+}, and this percentage decreased to 67% after annealing for 75 mins. The remaining portion of V (24% and 33%, respectively) was present as V^{5+}. The oxidation states were determined both from the $V2p_{3/2}$ binding energy as well as the difference between the $V2p_{3/2}$ and O1s binding energies. Taking the difference between these energies has been shown to be a favorable method for accurate chemical bonding state analysis [83]. Both techniques yielded the percentages shown in Fig. 4.2. This data elucidates that the sample surfaces consisted mostly of VO_2 with a minor component of V_2O_5. Deeper into the films the percentage of VO_2 was likely higher. Also, the deposited and 75 min annealed films represent the extremes of annealing time and therefore the other samples should fall within this range of stoichiometries. Later in this work, XRD data will be presented that shows the desired monoclinic VO_2 structure was obtained.

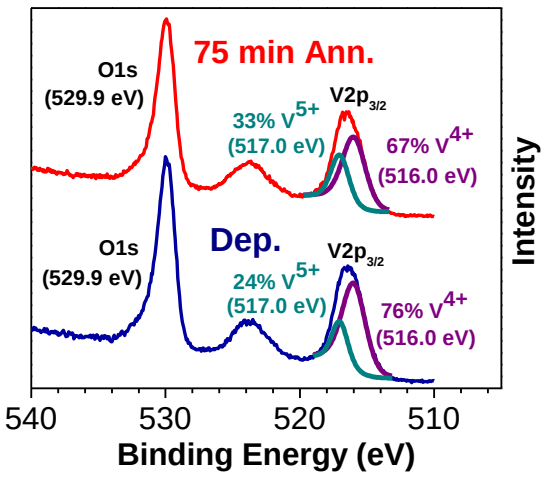

Fig. 4.2. High-resolution XPS spectra for as-deposited and 75 min annealed VO_2 films.

After the surfaces were characterized, optical transmittance was obtained with UV-Vis-NIR spectrophotometry. A representative transmittance spectrum is shown in Fig. 4.3 for the 45 min annealed sample. Data was collected at sample temperatures of 25 and 85 °C, respectively. Fig. 4.3 shows that the NIR transmittance decreased significantly by raising the sample temperature above τ_c, which indicates that thermochromism was achieved. The figure also shows that the transmittance of the sample was 35% at 500 nm and 58% at 570 nm for a sample temperature of 25 °C. With these optical properties, the color of the 45 min annealed film was light bronze. The 30, 60 and 75 min annealed samples were also light bronze; however the as-deposited and 15 min annealed samples were gray in appearance. Once the transmittance data was obtained, Eqn. (4.1) was used to calculate the UV, luminous and NIR transmittances for the samples. The results, summarized in Fig. 4.4, show that luminous transmittance increased from 37% as-deposited to 53% after annealing for 75 mins. Fig. 4.4 also indicates that the UV transmittance decreased from 22% as-deposited to 2% after annealing for 75 mins. This information shows the advantage of the optical performance metrics proposed in this work. The previous approach of calculating total solar transmittance would not have elucidated the decrease in UV transmittance observed in this study; yet this is a relevant piece of information given the design goal of limiting UV exposure for inhabitants in the built environment [6, 87]. Additionally, Fig. 4.4 shows the NIR transmittance for the samples measured at 25 and 85 °C, as well as the corresponding percent reduction by elevating the temperature above τ_c. The figure shows that the NIR transmittance of the 30 min annealed sample decreased by 23% (from 43 to 33%). This is nontrivial given that 52% of the total solar irradiance is in the NIR [59]. As annealing time was increased to 75 mins, the NIR percent reduction decreased to 15% (from 47 to 40%). Thus it is

concluded that either the 30 or 45 min annealing time was optimum in terms of low UV transmittance, relatively high luminous transmittance and NIR modulation.

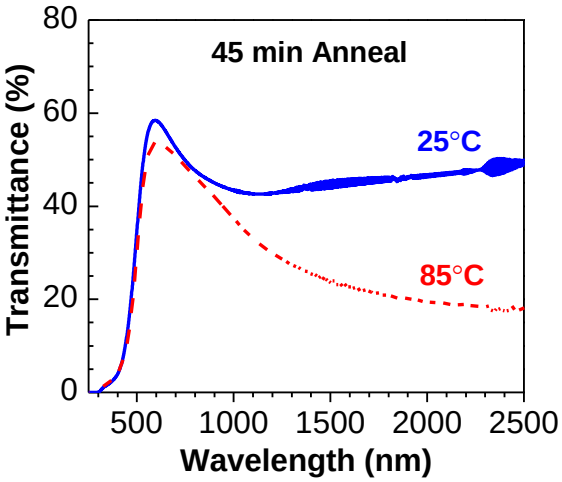

Fig. 4.3. Continuous UV-Vis-NIR transmittance for 45 min annealed VO_2 film at 25 and 85 °C, respectively.

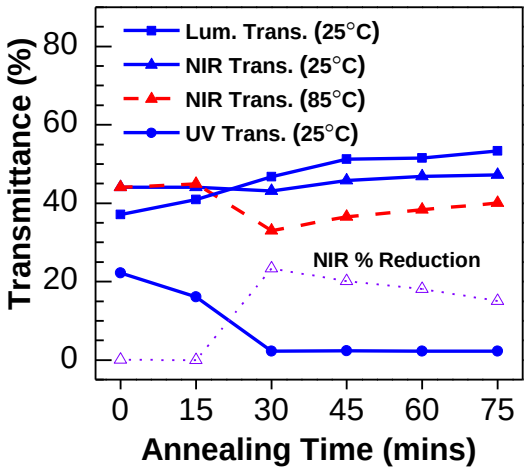

Fig. 4.4. UV, luminous and NIR transmittances for VO_2 samples with respect to annealing time. The purple line with unfilled triangles denotes the percent reduction in NIR transmittance due to raising the sample temperature from 25 to 85 °C. The percent reduction is calculated by taking the difference between transmittance values at a given annealing time and then dividing by the value at 25 °C. Not shown on the plot is a 10% reduction in luminous transmittance; i.e. from 51 to 47% for the 45 min annealed sample. The UV transmittance was unchanged when the sample was heated from 25 to 85 °C.

In addition to measuring transmittance from 250 to 2500 nm, it was also measured at a fixed wavelength of 2500 nm while the temperature was varied from 25 to 85 °C. This was done so that τ_c could be quantified by taking the derivative of transmittance with respect to temperature. A representative transmittance versus temperature plot is shown in Fig. 4.5(a) for the 45 min annealed sample, and the derivative of the curve is shown in Fig. 4.5(b). The results show a clear thermochromic transition with an average τ_c of 48 °C for the 45 min annealed sample. Hysteresis width in Fig. 4.5(b) can be determined by taking the difference between the critical transition temperatures in heating and cooling; thus the hysteresis width is approximately 8 °C for the 45 min annealed sample. The results for this characterization, summarized in Fig. 4.6, show that the average τ_c increased from 45 to 50 °C as the annealing time increased from 30 to 75 mins. The corresponding hysteresis widths for these samples increased from 6 to 12 °C as the annealing time was increased from 30 to 75 mins. From Fig. 4.6 it is concluded that the 30 min annealing time was optimum for achieving the lowest τ_c (45 °C).

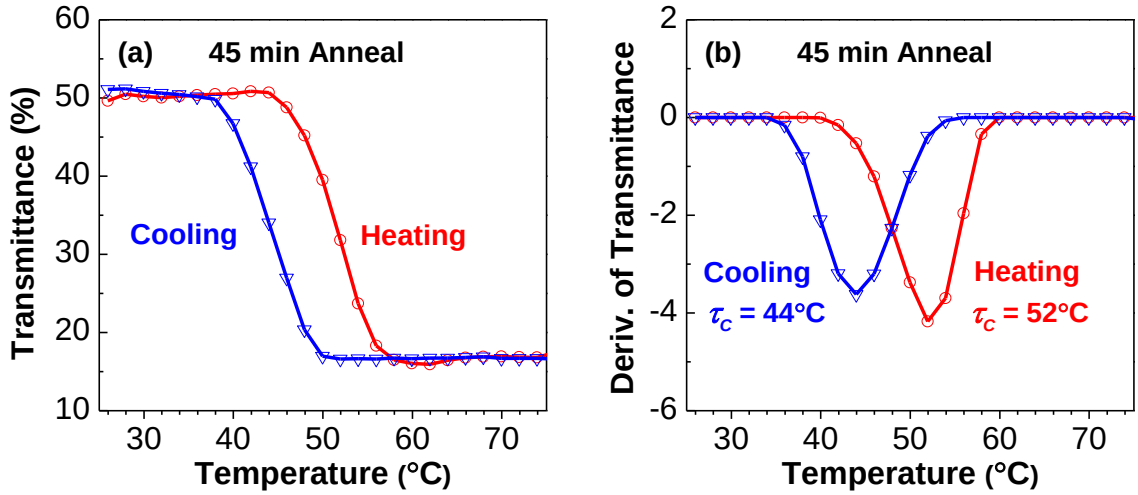

Fig. 4.5. (a) Transmittance of 45 min annealed VO_2 film at fixed wavelength of 2500 nm. (b) Derivative of transmittance curve. The transition temperatures in heating and cooling are indicated on the derivative figure.

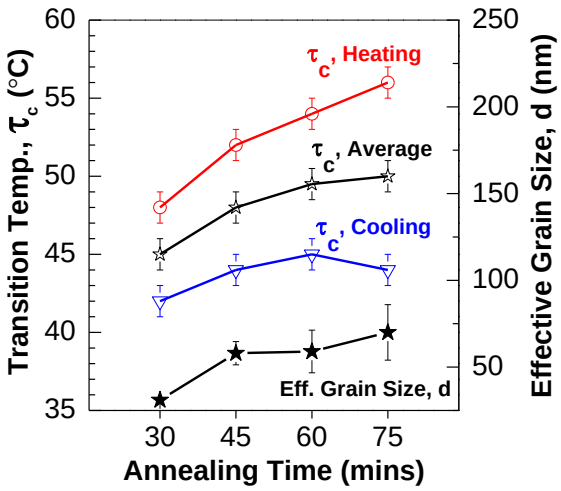

Fig. 4.6. Summary of transition temperature and effective grain size versus annealing time. Note the increase in both the average transition temperature and effective grain size as the annealing time is increased from 30 to 75 mins.

The samples in this study were also characterized with XRD for two main reasons: first to verify that monoclinic VO_2 was obtained, and second to enable quantitative estimation of grain size (qualitative estimation was achieved with SEM). The full set of XRD spectra are provided in Fig. 4.7. The underlying curvature shown in the figure is due to the glass substrate. The important features are the VO_2 reflections indicated on the figure. The results show that the deposited and 15 min annealed films were amorphous, and the 30, 45, 60 and 75 min annealed films possessed the monoclinic VO_2 structure. XRD scans were performed at sample temperatures of 25 and 95 °C, so that the phase transformation could be observed. Representative spectra are shown in Fig. 4.8 for the 45 min annealed sample. Fig. 4.8(a) shows that monoclinic reflections were obtained at 25 °C and rutile tetragonal reflections were obtained at 95 °C. Vertical lines in the figure correspond to reference data for VO_2 [25, 88]. The change in diffraction angles associated with the SMT is quite subtle and therefore a detail view centered at 2θ of 28° is provided in Fig. 4.8(b). The fact that the phase change from monoclinic to rutile was

reversible confirms that the desired thermochromic VO_2 was produced. Once XRD peaks were obtained for the crystalline samples, effective grain size was estimated using the monoclinic $(\bar{2}11)$ plane and the Scherrer equation. In this work, the word "effective" is added to grain size since the crystallites are generally not spheroidal and therefore the length calculated by the Scherrer equation does not directly yield the grain dimensions. However, both the magnitude and coarsening trend of the calculated effective grain sizes roughly agree with the SEM morphologies shown in Fig. 4.1. The grain size results, summarized in Fig. 4.6, show that the effective grain size increased from 31 to 70 nm by increasing the annealing time from 30 to 75 mins. Thus the 30 min annealing time resulted in the finest microstructure of crystalline VO_2.

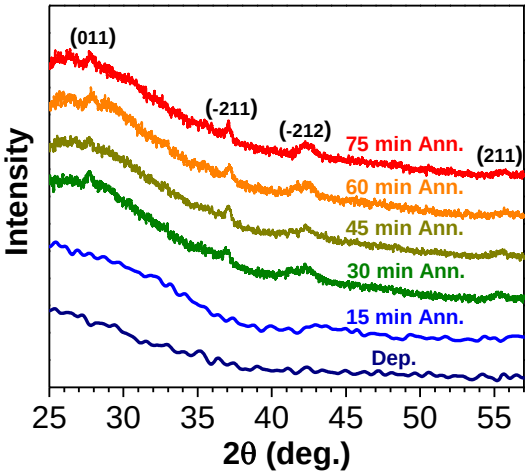

Fig. 4.7. XRD spectra for VO_2 films on glass. The peaks indicated in the figure correspond to monoclinic VO_2 [25].

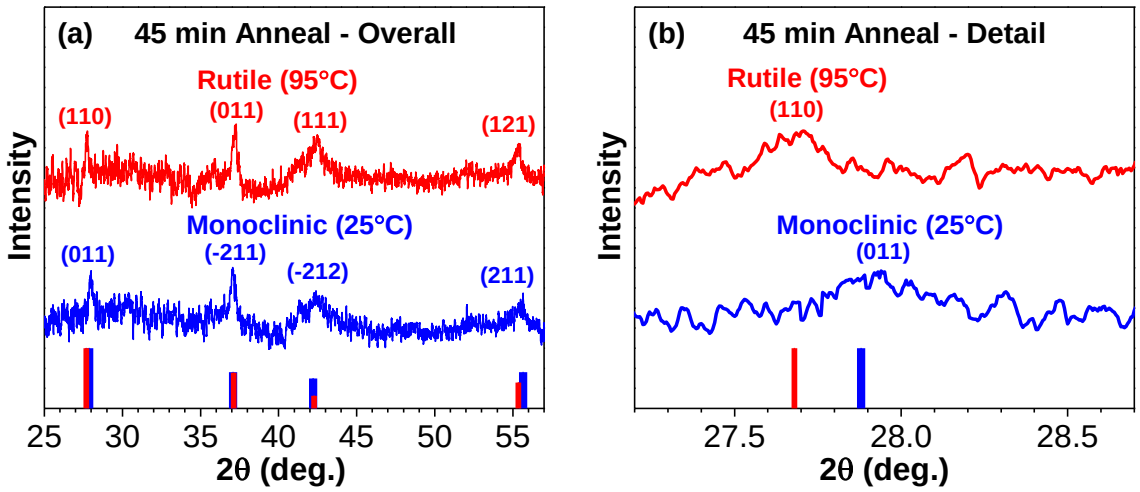

Fig. 4.8. XRD pattern of 45 min annealed VO_2 on glass. The background has been subtracted to enable closer inspection of the VO_2 peaks. (a) Overall view of data. (b) Detail view of $2\theta = 28°$ from overall view. The separation between the peaks in the detail view indicates the reversible phase transformation from monoclinic to tetragonal rutile. The vertical lines correspond to reference data for VO_2 [25, 88].

The data in this work display a trend where τ_c decreases concurrently with effective grain size and annealing time. Smaller grains result in a higher density of grain boundaries, and it appears that grain boundaries serve as nucleating defects which lower the activation energy required for the semiconducting-to-metallic transition. Furthermore, a high density of grain boundaries (small grain size) appears to reduce the hysteresis width of the transition. This is shown in Fig. 4.6 as a convergence between the transition temperatures in heating and cooling as the annealing time is reduced from 75 to 30 mins.

In the literature, the exact role of grain size on hysteresis is somewhat controversial due to complicating factors such as defects within a grain, grain shape and the inherent uncertainty in experimental techniques used to quantify d and τ_c [75]. It is widely known and accepted that τ_c of the bulk monocrystalline form of VO_2 is 67 to 68 °C and that the thin film form of the material tends to have a lower τ_c than the bulk . However, hysteresis in VO_2 is not fully

understood. For bulk single crystals of VO_2, some researchers have observed less than 1°C hysteresis width [91, 92] while others have observed 6 to 25 °C hysteresis width [11, 12, 93]. Thus the intrinsic hysteresis of bulk VO_2 is not widely agreed upon and there is no clear baseline by which to compare nanoscale forms of the material. The situation becomes even more complex for polycrystalline thin films, nanoparticles and other nanoscale forms of the material. In these configurations there appear to be two dominant parameters for controlling hysteresis – density of grain boundaries and density of defects within a grain (sometimes referred to specifically as crystallinity). Generally the latter has been regarded as reducing the hysteresis width in VO_2 [61]. However, there are apparently conflicting studies regarding the former in which increasing grain size has been shown to increase hysteresis [61] or decrease hysteresis [75]. For a continuous thin film, it would seem that a higher density of grain boundaries (smaller grain size) would increase the availability of nucleating defects which would in turn reduce hysteresis, and indeed that is suggested by the results in this study.

In summary, the current study shows that a small grain size is desirable for achieving a low τ_c and small hysteresis width; however there is also a lower limit to grain size such that crystallinity must be achieved to enable thermochromism. Fig. 4.4 shows that the as-deposited and 15 min annealed samples were not thermochromic, and this was due to an absence of crystallinity. This work shows that grain size has an important impact on both the transition temperature and hysteresis properties of vanadium dioxide. In general as the grain size increases, the transition temperature will increase and the hysteresis width will likely increase as well.

4.5 Conclusions

In this study the effect of grain size on the transition temperature of VO_2 has been investigated. The results show that τ_c of 45 °C can be achieved for an undoped VO_2 film by restricting effective grain size to approximately 30 nm. It is concluded that a higher density of grain boundaries (smaller grain size) provides a greater number of nucleating defects which in turn reduces τ_c. Similarly, a higher density of grain boundaries tends to reduce the hysteresis width. Also in this study a new set of optical performance metrics was proposed in which the solar spectrum was divided into the UV, visible and NIR regions. This approach is more closely aligned with the goals of limiting UV, enabling luminous and modulating NIR transmission. Using these metrics, the optical properties of the low-τ_c sample were: 2% UV transmittance, 47% luminous transmittance and 23% NIR modulation (decrease from 43 to 33%). The results demonstrate that the grain size of VO_2 should be viewed as an important parameter for controlling the transition temperature of the material.

5 Multilayer ITO/VO_2/TiO_2 Thin Films for Control of Solar and Thermal Spectra

5.1 Overview

In this study, a multilayer thin film of ITO/VO_2/TiO_2 was investigated for the control of solar and thermal spectra with potential application as an energy-efficient coating for windows in built environments. The functions for these layers were: low emissivity, thermochromism, and anti-reflectance in the visible region. Films were deposited using reactive magnetron sputtering and characterized with scanning electron microscopy, X-ray diffraction, X-ray photoelectron spectroscopy, UV-Vis-NIR spectrophotometry, and Fourier transform infrared spectroscopy. The results demonstrate that relatively high luminous transmittance, low emissivity, and favorable thermochromism can be achieved for a film with a transition temperature centered at 52 °C with a hysteresis width of 18 °C. This shows that an advancement of the previous state of the art can be made by restricting the Scherrer grain size of the VO_2 layer to 92 nm.

5.2 Introduction

More than 40% of primary energy in the U.S. is used in buildings and this usage is projected to continue for the foreseeable future [1]. Given that windows are a major pathway for energy losses from buildings, one way to improve energy efficiency is through the application of coatings with suitable properties. In temperate climates it is desirable that the optical properties of such window coatings can vary in response to a stimulus (chromogenic thin films). In this way the material can control the propagation of light depending on the conditions of the environment. One class of chromogenic coatings, thermochromic, changes optical properties in response to temperature. These materials could potentially be inexpensive relative to other technologies such as electrochromic coatings, because of their simplicity (i.e. one layer of material without the need for an applied voltage).

Vanadium(IV) oxide is an interesting thermochromic material because its transmittance in the visible region is relatively high and constant with temperature; however, its transmittance in the infrared region decreases significantly when the material is heated above its transition temperature (τ_c). Therefore, a thin layer of VO_2 could be used to control solar irradiance for windows in built environments. The change in optical properties is associated with a phase transition from a semiconducting monoclinic to a metallic rutile structure [12]. A major technical challenge for this material is that τ_c in the bulk monocrystalline form is about 67 to 68 °C [11, 26]. In the polycrystalline thin film form, τ_c appears to be closer to 55 °C [7, 18, 62] although some researchers have reported values up to 68 °C [86]. Some previous studies have shown that τ_c can be altered by about 5 °C by varying the grain size of VO_2 [18, 61]. The advantage of this approach compared to doping the material with a cation such as W^{4+} [27] is that it does not reduce the luminous transmittance (T_{lum}) and thermochromism of VO_2 [18]. High T_{lum} is

important for transmitting daylight into buildings. T_{lum} can be increased by applying a suitable anti-reflective layer (such as TiO_2) to the VO_2 [7, 10, 31, 78, 94].

The energy-efficient potential of VO_2 could be further enhanced through the application of a low emissive (low-E) material. Low-E coatings act as "hot mirrors," reflecting mid-IR radiation but transmitting most of the visible light [95]. These optical properties can be used to control the flow of thermal radiation (i.e. 5 to 10 μm). One class of high-performing low-E films is transparent conducting oxides (TCOs). Examples of TCOs include F_xSnO_{2-x} and $(SnO_2)_x(In_2O_3)_{1-x}$ [96]. TCOs are favorable for low-E because they have a wide optical band gap which enables high luminous transmittance, yet they also have free carriers which can reflect lower-energy photons in the thermal spectrum. By combining thermochromic and low-E materials into a multilayer design, both solar and thermal spectra can be controlled. One such study was performed through the synthesis and characterization of a multilayer $FTO/VO_2/TiO_2$ coating [78]. While that study demonstrated an innovative multilayer design, it also possessed a transition temperature centered at 71 °C with a hysteresis width of 17.4 °C [78]. For practical application of VO_2, it is desirable to lower τ_c close to room temperature (less than 25 °C). Furthermore, the luminous transmittance (T_{lum}) in [78] was about 44%, and it is desirable to raise T_{lum} to 55% or more for daylighting purposes in buildings [6]. Thus, there are technical challenges that need to be overcome before these multilayer systems can be utilized for energy efficiency.

In the current study, multilayer $ITO/VO_2/TiO_2$ samples are synthesized to achieve low emissivity, thermochromism, and visible anti-reflectance. The results show that these properties can be combined while still achieving a transition temperature centered at 52 °C with a hysteresis width of 18 °C. Moreover, T_{lum} of 56% is obtained through precise design and synthesis of the

multilayer system. This work demonstrates that an advancement in τ_c can be made by restricting the Scherrer grain size of the VO_2 layer to approximately 92 nm.

5.3 Materials and Methods

The goal of this work was to synthesize multilayer films with low emissivity, thermochromism and a relatively low (less than 55 ºC) transition temperature. The following steps were performed to achieve this goal. First, approximately 100 nm thick VO_2 films were reactively sputtered on glass substrates using a procedure that has been reported elsewhere [18]. The refractive indices of these films were characterized using a Woollam M-2000 spectroscopic ellipsometer. Both transmittance and reflectance measurements were performed with the ellipsometer to obtain a highly accurate index of refraction. A basis spline (B-Spline) method was used to determine the optical properties from the measured amplitude and polarization [97]. The B-Spline layer enables a high degree of flexibility in determining the complex index of refraction versus wavelength. This is achieved by specifying the optical constants at a number of control points which are equally spaced in photon energy. The values of the optical constants are then adjusted to reconstruct the measured amplitude and polarization with the B-Spline model. Values of the optical constants between control points are interpolated. Thus, the B-Spline layer is a very flexible approach for modeling the refractive index and it is especially useful for partially absorbing materials such as the VO_2 and ITO films used in this study. Next, the refractive index of the VO_2 was used as an input parameter for the program TFCalc by Software Spectra, Inc. TFCalc is used to simulate the optical performance of thin films and it has functionality for designing and optimizing anti-reflective coatings. Required inputs for the program include refractive index and layer thickness. A three layer structure of ITO/VO_2/TiO_2

was simulated with the program. The refractive index of TiO_2 was taken directly from the library of available materials included with TFCalc [98] and was verified to accurately model the behavior of single-layer TiO_2 on glass. The refractive index of ITO was obtained through ellipsometry, as mentioned above for VO_2. The thickness of the TiO_2 layer in the three-layer structure was numerically optimized to achieve minimum reflectance in the visible region (400 to 700 nm).

After the multilayer design was optimized, the next step was to synthesize the structure. Commercially-available ITO glass was used as the substrate (VisionTek Systems Ltd.). VO_2 was deposited on the ITO layer using the procedure referenced above [18]. The samples were then annealed in air at 365 ºC for 30 min using a Barnstead Thermolyne 47900 furnace. After the first annealing process was completed, the samples were returned to the sputtering system and a layer of TiO_2 was deposited on the samples. The procedure for the TiO_2 deposition process can be found in a previous publication [99]. The TiO_2 deposition process in this study had some slight differences from the one cited above, as follows. The sputtering power was 100 W, the deposition time was 7.75 min and the substrate was maintained at room temperature. These parameters were selected to produce a 34 nm thick TiO_2 layer, which was chosen based on the results of the TFCalc simulation. Following the TiO_2 deposition, the samples were annealed for a second time at 365 ºC. The second annealing process was conducted for 15, 30, and 45 min, respectively. Therefore, in this study the VO_2 and TiO_2 layers were annealed for different lengths of time. The relationship between the two is: $x_1 = x_2 + 30\ min$, where x_1 and x_2 are the VO_2 and TiO_2 annealing times in minutes, respectively. This two-step annealing process was used because it was found to produce a higher level of thermochromism than annealing the multilayer film in a single step.

Naturally-fractured cross sections of the films were characterized with an FEI Sirion scanning electron microscope (SEM). The working distance for SEM was 5 mm, the accelerating voltage was 5 kV, and the scan was performed in ultra-high resolution mode. Next, crystallinity of the samples was characterized with X-ray diffraction (XRD) using a Bruker D8 Discover with GADDS. Cu K_α was used as the radiation source for XRD, and data was collected from 2θ of 15 to 70°. After XRD spectra were obtained, crystalline grain size was estimated using the full-width at half-maximum (FWHM) of the monoclinic (011) peak and the Scherrer equation [25, 89]

$$d = \frac{K\lambda}{(\beta - \beta_0)\cos\theta} \tag{5.1}$$

where d is the grain size, K is a dimensionless shape factor assumed to be 0.9, λ is the wavelength of the radiation source (0.154184 nm), β is the measured FWHM (in radians), β_0 is a correction factor to account for instrumental broadening and θ is the Bragg angle. The value of β_0 was estimated to be 0.00232 rad (0.133°) based on an LaB_6 standard [90]. The FWHM was measured using the built-in functions of the DIFFRAC.EVA 3.0 software.

Chemical compositions of the as-deposited and 45 min annealed TiO_2 layers were characterized with high-resolution X-ray photoelectron spectroscopy (XPS) using a Kratos AXIS Ultra. Monochromatic Al K_α was used as the radiation source for XPS, and the data was analyzed with CasaXPS 2.3.15. The spectra were corrected by setting the C 1s binding energy to 284.6 eV, which is common practice for XPS analysis [52].

Transmittance of the films was obtained with UV-Vis-NIR spectrophotometry using a Varian Cary 5000. The measurement was performed between wavelengths of 250 and 2500 nm. The following equation was used to integrate the data into three scalar values which can be used to compare different samples in a quantitative and objective way [18]:

$$T_{reg.}(\tau) = \int \varphi_{reg.}(\lambda) T(\lambda, \tau) d\lambda \,/\, \int \varphi_{reg.}(\lambda) d\lambda \quad (5.2)$$

where λ is the wavelength of the incident light, $\varphi_{reg.}$ is a weight function for a region, τ is the sample temperature and T is transmittance. Three regions were used as domains of integration: UV $(250 < \lambda < 400\, nm)$, visible $(400 < \lambda < 700\, nm)$, and NIR $(700 < \lambda < 2500\, nm)$. For the UV and NIR regions, the AM1.5 spectrum was used for φ [85]. For the visible region, the luminous efficiency of the light-adapted eye was used for φ [84]. An additional spectrometry measurement was performed in which the wavelength was fixed at 2500 nm, and the temperature was cycled from 25 to 85 °C in 2 °C increments. The derivative of this measurement was calculated, and the temperature corresponding to the maximum magnitude was defined as the critical transition temperature (τ_c). Lastly, emissivity of the samples was determined using a PerkinElmer RXI Fourier transform infrared (FTIR) spectrometer. The FTIR was used to measure both transmittance and reflectance of the samples at a wavelength of 10 μm. Therefore absorptance could be determined separately from reflectance, and emissivity was considered equal to absorptance based on Kirchhoff's radiation law. The procedure in this study enabled the synthesis and characterization of high-performing multilayer thin films which combined thermochromism, low emissivity, and anti-reflectance. Furthermore, the transition temperature was modified by varying the annealing time and grain size of the samples.

5.4 Results and Discussion

In this work, a commercially-available ITO glass (VisionTek Systems Ltd.) was used as a substrate for producing VO_2/TiO_2 thin films. The thickness of the glass was 1.1 mm. The ITO layer was approximately 155 ± 7 nm thick, which was determined from cross-sectional SEM characterizations. The sheet resistance of the ITO was about 12 Ω/sq. A 100 ± 5 nm thick VO_2

film was deposited on the ITO glass substrate. This thickness was chosen because it resulted in a luminous transmittance (T_{lum}) of more than 55% and NIR modulation (thermochromism) of more than 16%. For window coatings, it is desirable for T_{lum} to be at least 55% to allow daylight to be transmitted into buildings [6]. Thicker films of VO_2 can yield more NIR modulation, but the disadvantage is that they also absorb more light in the visible region [82]. The top layer of the three layer structure, TiO_2, was numerically optimized at 34 nm to achieve minimum reflectance in the visible region. Fig. 5.1(a) shows the simulated transmittance of the ITO, ITO/VO_2, and ITO/VO_2/TiO_2 thin films. Note that the spectra terminate at 1700 nm because that is the limit of the Woollam M-2000 spectroscopic ellipsometer which was used to determine the refractive indices of the ITO and VO_2 layers. The experimentally-observed transmittance is shown in Fig. 5.1(b) for comparison. The visible region, plotted as an inset figure, shows a small but non-trivial increase in transmittance. The predicted behavior agrees reasonably well with the experimental data in the UV and visible regions; however, the NIR region had more discrepancy. The source of this discrepancy is not entirely clear but it appears to be related to the simulation not fully capturing the reduction in NIR reflectance from ITO glass that occurs when a VO_2 film is deposited on the substrate. For example, at 1700 nm the simulation predicts a transmittance of 28% for the ITO/VO_2 film, but the experimental value is 46%. In spite of the discrepancy in the NIR region, the simulation was successful in modeling and optimizing transmittance in the visible region as shown in the inset of Fig. 5.1. Therefore, it was determined that the simulation was effective for this purpose.

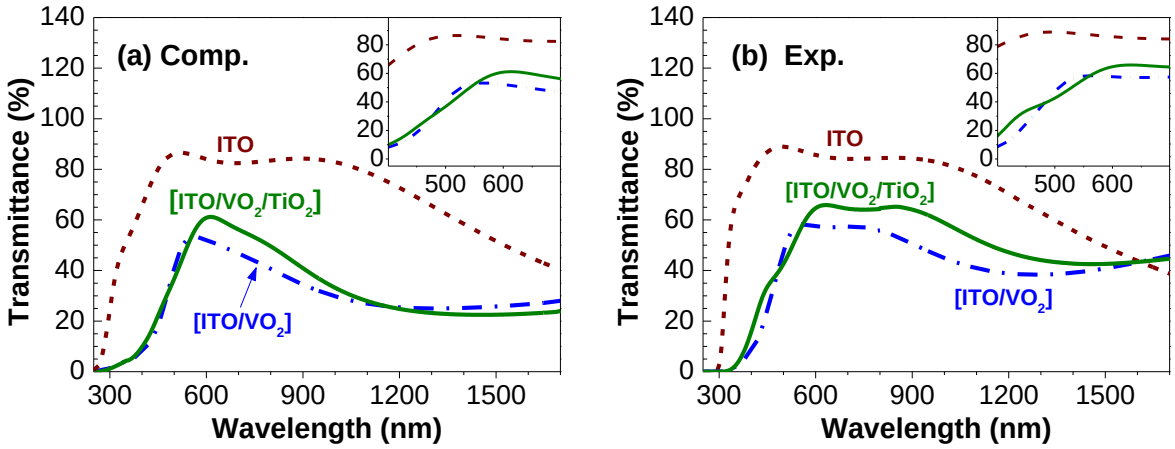

Fig. 5.1. (a) Computational and (b) experimental transmittance of ITO/VO_2 film with and without a TiO_2 anti-reflective layer. Transmittance of the uncoated ITO glass substrate is shown as a red dashed line. For the three-layer structure, the thickness of the TiO_2 coating was numerically optimized to achieve minimum reflectance in the visible region (inset figure).

To verify that the desired layer thicknesses were achieved, naturally-fractured cross sections of the samples were characterized with SEM. The SEM images, provided in Fig. 5.2, show that layer thicknesses were approximately 155 ± 7 nm, 100 ± 5 nm, and 34 ± 4 nm for ITO, VO_2, and TiO_2, respectively. Thus the desired multilayer structure was synthesized using the approach described in Section 2. The results show that the films were generally uniform and smooth; which is common for films deposited with magnetron sputtering [18]. These characteristics make magnetron sputtering a favorable technique for depositing optical coatings, such as the multilayer films in this study. Cross sectional morphologies of the samples appeared to be mostly equiaxial. Microstructures of the samples were characterized with XRD, and the results are shown in Fig. 5.3. The characterization confirmed that the 155 ± 7 nm ITO base layer had relatively high crystallinity, meaning that numerous ITO peaks of strong intensity were detected. This is reinforced by considering the fact that the background appeared as mostly flat instead of showing the characteristic “hill” of uncoated glass. ITO peaks in Fig. 5.3 can be identified by

comparing with the bottom line in the figure, which shows the XRD reflections for the as-received substrate. VO_2 peaks in the figure are indicated by the diamond symbols above the top line. Vertical lines are shown at 2θ of 37.0º and 37.5º to help distinguish between a faint VO_2 $(\bar{2}11)$ peak and an ITO peak contributed from the substrate. The XRD results show that the as-deposited VO_2 film was amorphous, whereas the 30 to 75 min annealed films had the desired monoclinic structure.

Due to the thinness (34 nm) of the TiO_2 top-layer, it was difficult to detect crystallinity for this material. Therefore, high-resolution XPS was selected to characterize the TiO_2 layer. XPS results for the [ITO/VO_2 (30 min)/TiO_2 (dep)] and [ITO/VO_2(75 min)/TiO_2 (45 min)] samples are presented in Fig. 5.4. The results show that both samples comprised pure TiO_2. This was determined both from the binding energy of the Ti $2p_{3/2}$ peak (approximately 458.7 eV) [52], and by taking the difference between the Ti $2p_{1/2}$ and Ti $2p_{3/2}$ peaks (Δ = 5.74 eV). Both techniques indicated that the charge of the metal cation was Ti^{4+}. Therefore the desired TiO_2 top-layer was produced.

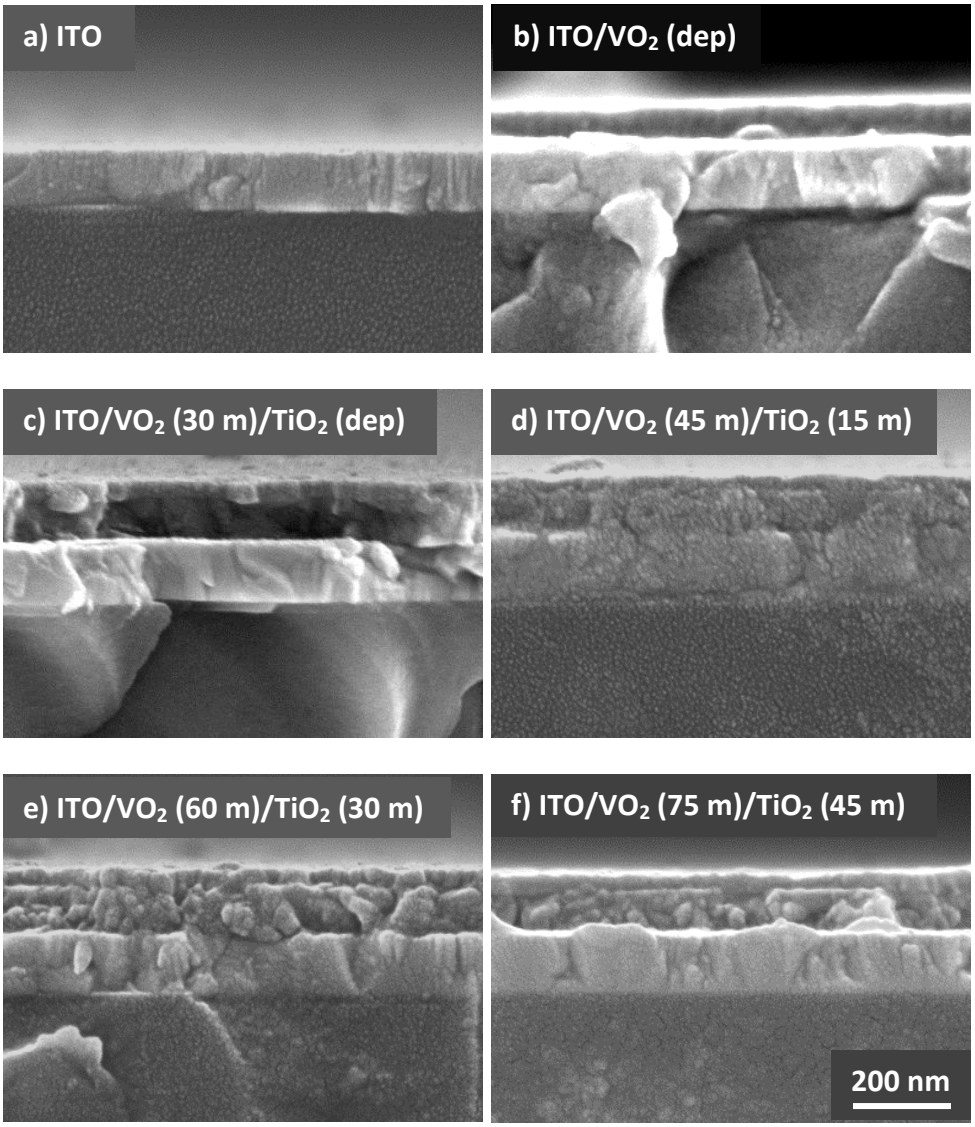

Fig. 5.2. Cross sectional SEM images of ITO, ITO/VO_2, and ITO/VO_2/TiO_2 films on glass substrates. Different annealing times for VO_2 and TiO_2 are indicated on the figure since annealing proceeded in a two-step process.

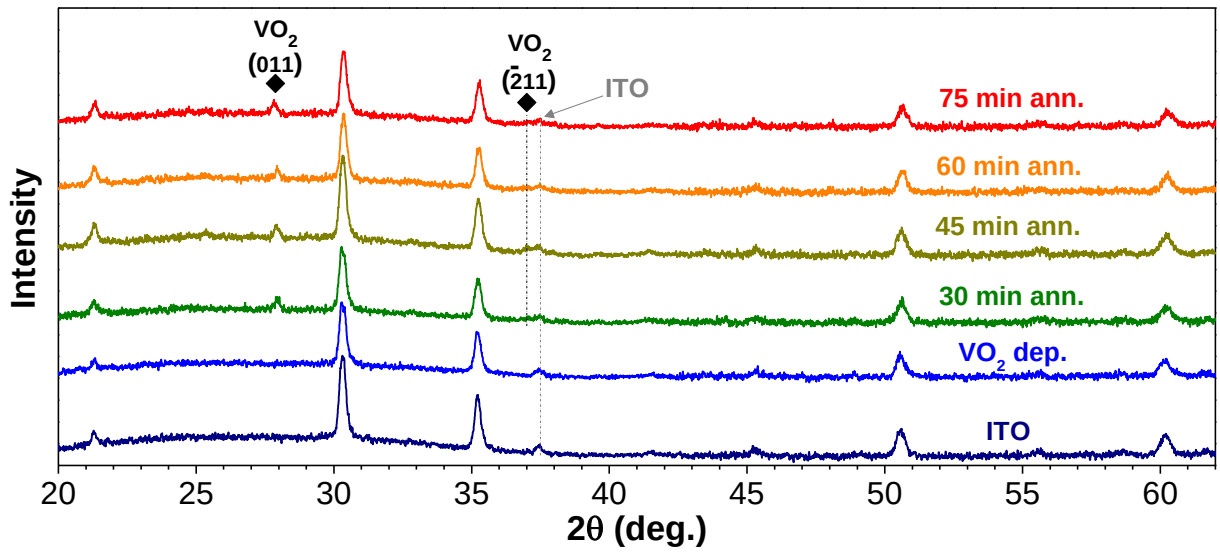

Fig. 5.3. XRD spectra for ITO/VO_2/TiO_2 films. The annealing times shown on the figure are for the VO_2 layer. TiO_2 annealing times can be determined by subtracting 30 min from the times shown.

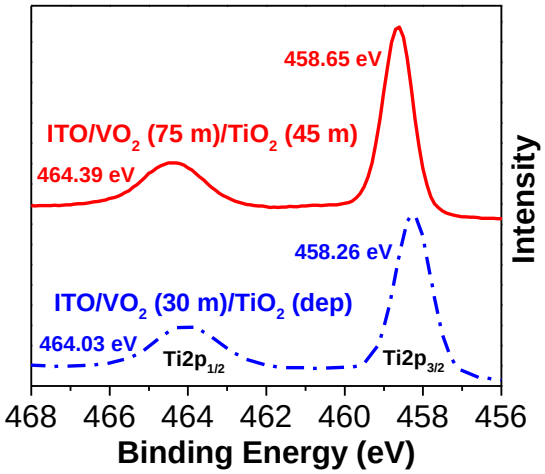

Fig. 5.4. High-resolution XPS data for multilayer films.

The samples were characterized with UV-Vis-NIR spectrophotometry to determine their optical properties. A representative transmittance spectrum is provided in Fig. 5.5 for the 60 min annealing time. The solid and dashed lines in the figure correspond to measurements performed at 25 ºC and 85 ºC, respectively. Some general features of the optical properties include

relatively high luminous transmittance and a reduction in NIR transmittance after the sample is heated above the transition temperature. These qualitative properties were analyzed quantitatively by applying Eqn. (5.2). The results of the calculations are presented in Fig. 5.6. In the figure, two X-axes for annealing time are shown as a reminder that the TiO_2 and VO_2 layers were annealed for different lengths of time. Fig. 5.6 shows that the NIR % reduction and UV transmittance were relatively constant with annealing time; however, the luminous and NIR transmittances increased with annealing time. Based on the results shown in Fig. 5.6, the 60 and 75 min annealing times had the most favorable luminous transmittance and NIR % reduction of the samples in this study.

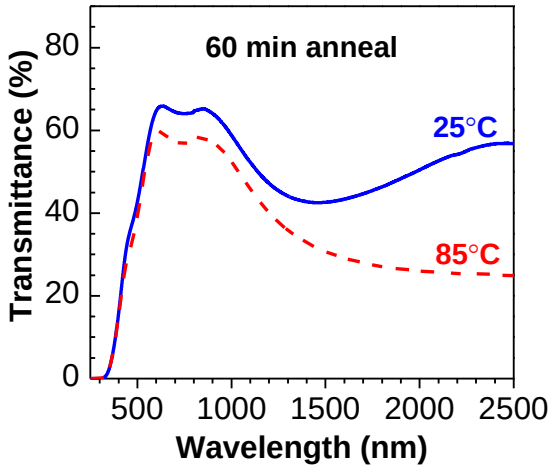

Fig. 5.5. Transmittance of [155 nm ITO / 100 nm VO_2/ 34 nm TiO_2] 60 min annealed film measured above and below the transition temperature.

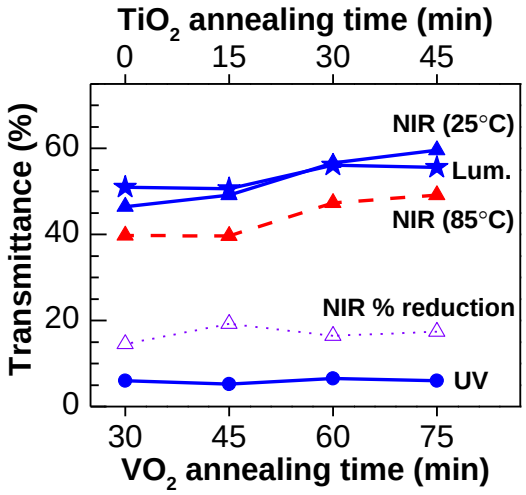

Fig. 5.6. Integrated transmittances of ITO/VO_2/TiO_2 multilayer films. NIR % reduction was calculated by taking the difference between NIR transmittance values at a given annealing time and then dividing by the value at 25 ºC.

The transition temperatures of the samples were determined by fixing the wavelength of the spectrophotometer at 2500 nm and varying the temperature from 25 to 85 °C. The results for the 60 min annealed sample are shown in Fig. 5.7(a). By taking the derivative of transmittance with respect to temperature, the critical transition temperatures (τ_c) of the samples were determined. It is important to note that for hysteretic samples, two transition temperatures are obtained; one in heating ($\tau_{c,h}$) and one in cooling ($\tau_{c,c}$). In the literature, there are generally two approaches for describing τ_c of hysteretic samples. The first is to simply provide both $\tau_{c,h}$ and $\tau_{c,c}$ [7, 61, 62]. The other approach is to calculate the average between these two values and then provide the hysteresis width (difference between $\tau_{c,h}$ and $\tau_{c,c}$) [18, 27, 28, 78]. In the current work, the authors have chosen the latter approach for conciseness. Specifically, the transition temperature is defined here as $\tau_c = \frac{(\tau_{c,h}+\tau_{c,c})}{2} \pm \frac{(\tau_{c,h}-\tau_{c,c})}{2}$ (average $\tau_c \pm$ half of hysteresis width). The results of this analysis, presented in Fig. 5.7(b), show that τ_c was 52 ± 9 °C for the 60 min annealed sample. Data for the other annealing times are summarized in Fig. 5.8, which shows that τ_c

increased from 49 ± 9 °C to 53 ± 9 °C as the VO_2 annealing time increased from 30 to 75 min. Thus, the 30 min annealing time resulted in the lowest average transition temperature for the samples in this study. The increase in τ_c with annealing time for the multilayer films was also observed for a separate set of single-layer VO_2 films [18], which helps to establish confidence in the trend. In addition to τ_c, Scherrer grain size (d) is also plotted in Fig. 5.8. The grain size was calculated by measuring the FWHM of the VO_2 (011) peak and inputting the value into Eqn. (5.1). As Fig. 5.8 indicates, d increased from approximately 42 to 112 nm as the VO_2 annealing time increased from 30 to 75 min. Therefore, both the transition temperature and the Scherrer grain size increased as a result of the post-deposition annealing process.

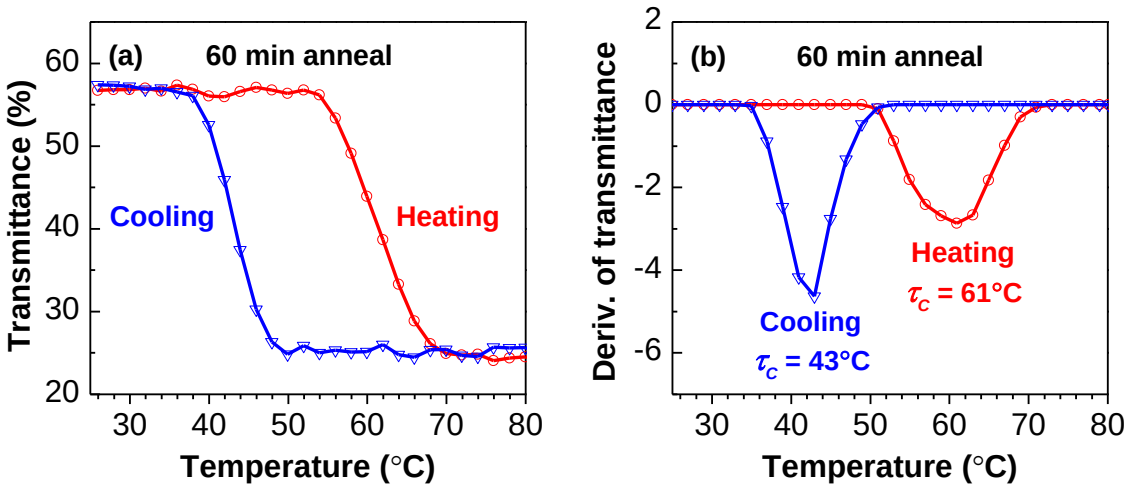

Fig. 5.7. (a) Transmittance at fixed wavelength of 2500 nm for 60 min ITO/VO_2/TiO_2 sample. (b) Derivative of transmittance with respect to temperature.

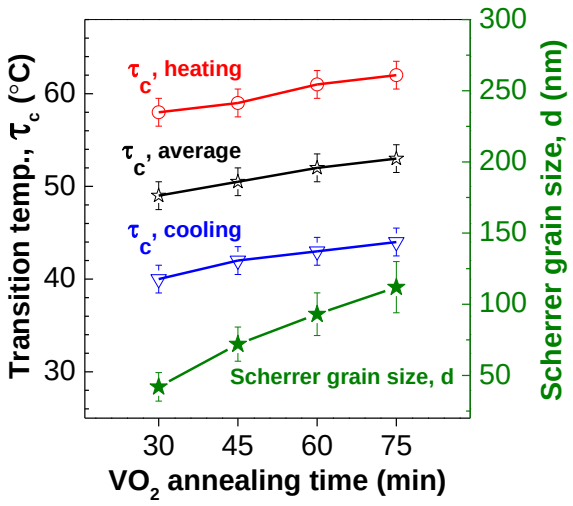

Fig. 5.8. Summary of VO_2 transition temperature and Scherrer grain size versus annealing time.

Emissivity of the multilayer samples was characterized at a wavelength of 10 µm using an FTIR spectrometer. VO_2/TiO_2 films on both ITO glass and common PS (potash-soda) glass were characterized to determine how much the emissivity was influenced by the presence of the ITO layer. PS glass is a type of common silica glass with higher thermal stability than soda lime, which makes it suitable for producing VO_2 films [82]. The emissivity of the PS glass is not significantly different from other silica glasses, and therefore it can be used for comparison with ITO-coated silica glass. The results, presented in Fig. 5.9, show that a slight increase in emissivity with annealing time was detected; however, it did not exceed the uncertainty in the characterization for a given substrate type. By contrast, the VO_2/TiO_2 film on ITO glass did have a significantly lower emissivity (0.26 compared to 0.68) than the film on PS glass. The FTIR data verifies that the multilayer structure with ITO had a much lower emissivity than the structure without the ITO layer.

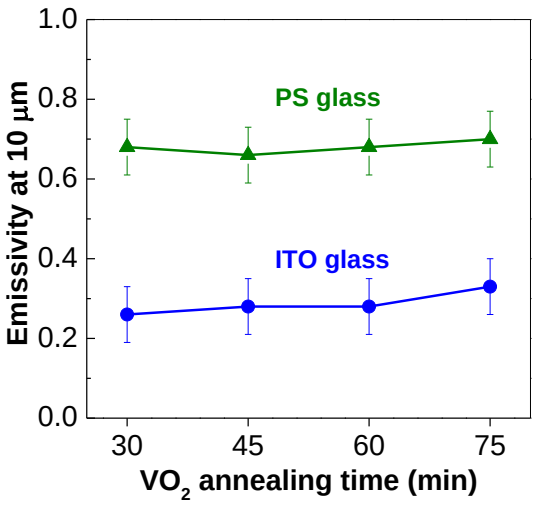

Fig. 5.9. Emissivity determined at wavelength of 10 µm for VO_2/TiO_2 on PS and ITO glass substrates.

In summary, the ITO/VO_2/TiO_2 films in this study combined thermochromism, low-emissivity and visible anti-reflectance. Specifically, the luminous transmittance of the 60 min annealed sample was 56.1%, the NIR % reduction was 16.5% (from 59.6 to 49.2%), and the emissivity of the sample was 0.28. These optical properties generally match or exceed those of the previous state of the art for a low-E / thermochromic multilayer thin film [78]. Moreover, the transition temperature of the sample in the current study was approximately 52 ± 9 °C. τ_c could be further lowered to 49 ± 9 °C by shortening the annealing time to 30 min and reducing the grain size to 42 nm. However, the shorter annealing time resulted in a reduction in T_{lum} due to the as-deposited TiO_2 layer having a non-zero extinction coefficient. The main advancement in this work compared to the previous state of the art is that τ_c in the earlier study was 71 ± 9 °C [78]. The lower transition temperature of 52 ± 9 °C in this work appears to be associated with limiting the Scherrer grain size to 92 nm. These findings are important because they demonstrate that visible anti-reflectance and low emissivity can be achieved while keeping the transition temperature of VO_2 relatively low through the grain size reduction approach. The

thermochromism of VO_2 can potentially be applied to control solar irradiance and the low emissive layer can be used to control the thermal spectrum for windows in built environments and automobiles.

5.5 Conclusions

This study shows that the potentially energy-efficient properties of thermochromism and low emissivity can be combined using a three-layer structure of ITO/VO_2/TiO_2. Furthermore, the transition temperature of the VO_2 layer was limited to 52 ± 9 °C by restricting the Scherrer grain size to 92 nm. The luminous transmittance of the sample was 56.1% and its NIR % reduction was 16.5% (from 59.6 to 49.2%). Emissivity of the multilayer thin film was about 0.28. These properties constitute an advancement of the state of the art because they are accompanied by a significantly lower transition temperature than was previously reported for a thermochromic / low-E system. With further advancement, the multilayer thin film in this study could be used to control solar and thermal spectra for windows in built environments and automobiles.

6 Summary

6.1 Final Remarks

In this dissertation energy-efficient coatings have been investigated through experimental and numerical investigations. A multilayer structure of ITO/VO_2/TiO_2 was designed, synthesized and characterized. The purposes for these layers were low emissivity, thermochromism, and anti-reflectance in the visible region. Individual studies for TiO_2 and VO_2 were presented in Chs. 2 and 3 - 4, respectively. The work in Ch. 2 showed that the mechanical properties of TiO_2 can be controlled independently of the optical and electrical properties by varying synthesis temperature. This knowledge is important because TiO_2 is often used as the outer-most layer in optical devices including the thermochromic smart window investigated in this dissertation. In Ch. 3, it was shown that substrate composition can have a very strong impact on the structure and properties of vanadium oxide thin films. Sodium (Na) from the soda lime glass substrate undesirably inhibited thermochromism; however, replacing half of the Na with potassium (K) suppressed the Na diffusion and promoted the nucleation of pure VO_2 with superior thermochromism. The work in Ch. 4 showed that the transition temperature (τ_c) of VO_2 can be lowered from 50 to 45 °C by reducing the effective grain size of the film from 70 to 31 nm. Lastly, Ch. 5 demonstrated that the above knowledge can be combined with a low-E material to produce an excellent multilayer system with low emissivity, thermochromism, and anti-reflectance in the visible region. The multilayer represents an advancement in the state of the art because its optical properties generally match or exceed those of previous studies and τ_c in the current work is nearly 20 °C less than the previous benchmark for a low-E/VO_2 multilayer coating [78]. This dissertation contributes knowledge that helps reduce the barriers which

currently limit thermochromic materials from being utilized for energy efficiency in built environments.

6.2 Future Directions

The greatest technical challenge currently limiting the application of VO_2 as a smart window coating is that τ_c has not yet been lowered to room temperature without drastically reducing luminous transmittance and NIR modulation (thermochromism) [6, 27]. In this dissertation, τ_c was lowered to approximately 45 °C while still maintaining 47% luminous transmittance and 23% NIR modulation (decrease from 43 to 33%). The transition temperature will need to be further reduced in the future if VO_2 is to be used as a smart window coating for buildings. However, it is possible that with the current understanding of τ_c, VO_2 could be used for other applications such as switches [100], sensors [101], data storage [102], infrared modulators and more. Systems that utilize the unique properties of VO_2 will be interesting to watch in the coming years.

One research question that the author feels has not been fully answered in the literature is the exact effect of dopants on τ_c. Qualitatively it has been reported that W^{6+}, Mo^{6+}, Ta^{5+}, Nb^{5+} and Ru^{4+} are donor impurities that can decrease the transition temperature of VO_2 [26]. Moreover, Ge^{4+}, Al^{3+} and Ga^{3+} are acceptor impurities that can evidently increase τ_c [26]. However, Mg^{2+} has been reported to decrease τ_c of VO_2 [28]. This appears to contradict the aforementioned trend and the author of this dissertation has not seen a theoretical basis which clarifies the apparent contradiction. Moreover, this is an important question both for a fundamental understanding of this material, as well as for the practical consideration of reducing τ_c to a suitable level for the application of VO_2 in smart windows and other useful devices.

References

[1] U.S. Dept. of Energy, 2011 Buildings Energy Data Book, (2012).

[2] S. Biermann, A. Poteryaev, A.I. Lichtenstein, A. Georges, Phys. Rev. Lett., 94 (2005) 026404.

[3] C.G. Granqvist, S. Green, G.A. Niklasson, N.R. Mlyuka, S. von Kræmer, P. Georén, Thin Solid Films, 518 (2010) 3046-3053.

[4] C.C. Shih, C.M. Shih, K.Y. Chou, S.J. Lin, Y.Y. Su, R.A. Gerhardt, J. Biomed. Mater. Res. A, 82 (2007) 872-883.

[5] C. Ma, M. Taya, C. Xu, Polym. Eng. Sci., 48 (2008) 2224-2228.

[6] S.Y. Li, G.A. Niklasson, C.G. Granqvist, Thin Solid Films, 520 (2012) 3823-3828.

[7] P. Jin, G. Xu, M. Tazawa, K. Yoshimura, Appl. Phys. A-Mater., 77 (2003) 455-459.

[8] B.S. Richards, PhD Thesis. University of New South Wales, (2002).

[9] D.A.H. Hanaor, C.C. Sorrell, J. Mater. Sci., 46 (2011) 855-874.

[10] O.S. Heavens, Optical Properties of Thin Solid Films, Dover Publications, Inc., New York, 1991.

[11] F.J. Morin, Phys. Rev. Lett., 3 (1959) 34-36.

[12] M. Marezio, B. McWhan, P.D. Dernier, J.P. Remeika, Phys. Rev. B-Solid St., 5 (1972) 2541-2551.

[13] A. Cavalleri, T. Dekorsy, H.H.W. Chong, J.C. Kieffer, R.W. Schoenlein, Phys. Rev. B, 70 (2004).

[14] W.-T. Liu, J. Cao, W. Fan, Z. Hao, M.C. Martin, Y.R. Shen, J. Wu, F. Wang, Nano Let., 11 (2010) 466-470.

[15] W.W. Li, J.J. Zhu, J.R. Liang, Z.G. Hu, J. Liu, H.D. Chen, J.H. Chu, J. Phys. Chem. C, 115 (2011) 23558-23563.

[16] N. Sepúlveda, A. Rua, R. Cabrera, F. Fernandez, Appl. Phys. Lett., 92 (2008) 191913.

[17] K.-Y. Tsai, T.-S. Chin, H.-P.D. Shieh, Jpn. J. Appl. Phys., 43 (2004) 6268.

[18] M.J. Miller, J. Wang, J. Appl. Phys., 117 (2015) 034307.

[19] Y. Gu, J. Cao, J. Wu, L.-Q. Chen, J. Appl. Phys., 108 (2010) 083517.

[20] H. Guo, K. Chen, Y. Oh, K. Wang, C. Dejoie, S.A.S. Asif, O.L. Warren, Z.W. Shan, J. Wu, A.M. Minor, Nano Lett., 11 (2011) 3207-3213.

[21] C. Ko, S. Ramanathan, Appl. Phys. Lett., 93 (2008) 252101.

[22] A. Tselev, V. Meunier, E. Strelcov, W.A. Shelton, I.A. Luka'yanchuk, K. Jones, R. Proksch, A. Kolmakov, S.V. Kalinin, ACS Nano, 4 (2010) 4412-4419.

[23] Z. Yang, C. Ko, S. Ramanathan, J. Appl. Phys., 108 (2010) 073708.

[24] T. Yao, X.D. Zhang, Z.H. Sun, S.J. Liu, Y.Y. Huang, Y. Xie, C.Z. Wu, X. Yuan, W.Q. Zhang, Z.Y. Wu, G.Q. Pan, F.C. Hu, L.H. Wu, Q.H. Liu, S.Q. Wei, Phys. Rev. Lett., 105 (2010).

[25] Powder Diffraction Files, Card No. 00-009-0142, Database Edition, International Center for Diffraction Data (ICDD), Newton Square, PA 19073-3273, USA, (2012).

[26] J.B. Goodenough, J. Solid State Chem., 3 (1971) 490-500.

[27] T.D. Manning, I.P. Parkin, J. Mater. Chem., 14 (2004) 2554-2559.

[28] N.R. Mlyuka, G.A. Niklasson, C.G. Granqvist, Appl. Phys. Lett., 95 (2009) 171909.

[29] F. Wooten, Optical Properties of Solids, Academic, New York, NY, 1972.

[30] S.Z. Karazhanov, P. Ravindran, P. Vajeeston, A. Ulyashin, T.G. Finstad, H. Fjellvåg, Phys. Rev. B, 76 (2007) 075129.

[31] W. Kern, E. Tracy, RCA Rev., 41 (1980) 133-180.

[32] O. Carp, C.L. Huisman, A. Reller, Prog. Solid State Chem., 32 (2004) 33-177.

[33] V.V. Brus, M.I. Ilashchuk, Z.D. Kovalyuk, P.D. Maryanchuk, K.S. Ulyanytsky, B.N. Gritsyuk, Semicond., 45 (2011) 1077-1081.

[34] B. O'Regan, M. Grätzel, Nature, 353 (1991) 737-740.

[35] Y. Furubayashi, T. Hitosugi, Y. Yamamoto, K. Inaba, G. Kinoda, Y. Hirose, T. Shimada, T. Hasegawa, Appl. Phys. Lett., 86 (2005) 252101-252103.

[36] T. Hitosugi, N. Yamada, N.L.H. Hoang, J. Kasai, S. Nakao, T. Shimada, T. Hasegawa, Thin Solid Films, 517 (2009) 3106-3109.

[37] R. Asahi, T. Morikawa, T. Ohwaki, K. Aoki, Y. Taga, Science, 293 (2001) 269-271.

[38] B.R. Weinberger, R.B. Garber, Appl. Phys. Lett., 66 (1995) 2409-2411.

[39] A.S.M.A. Haseeb, M.M. Hasan, H.H. Masjuki, Surf. Coat. Technol., 205 (2010) 338-344.

[40] S. Schiller, G. Beister, W. Sieber, G. Schirmer, E. Hacker, Thin Solid Films, 83 (1981) 239-245.

[41] P. Zeman, S. Takabayashi, Surf. Coat. Technol., 153 (2002) 93-99.

[42] P. Löbl, M. Huppertz, D. Mergel, Thin Solid Films, 251 (1994) 72-79.

[43] M.H. Suhail, G.M. Rao, S. Mohan, J. Appl. Phys., 71 (1992) 1421-1427.

[44] R. Ananthakumar, B. Subramanian, S. Yugeswaran, M. Jayachandran, J. Mater. Sci.: Mater. Electron., 23 (2012) 1898-1904.

[45] J. Szczyrbowski, G. Bräuer, M. Ruske, J. Bartella, J. Schroeder, A. Zmelty, Surf. Coat. Technol., 112 (1999) 261-266.

[46] P. Frach, D. Glöß, K. Goedicke, M. Fahland, W.M. Gnehr, Thin Solid Films, 445 (2003) 251-258.

[47] O. Zywitzki, T. Modes, H. Sahm, P. Frach, K. Goedicke, D. Glöß, Surf. Coat. Technol., 180–181 (2004) 538-543.

[48] K.-R. Wu, C.-H. Ting, J.-J. Wang, W.-C. Liu, C.-H. Lin, Surf. Coat. Technol., 200 (2006) 6030-6036.

[49] Y. Gaillard, V.J. Rico, E. Jimenez-Pique, A.R. González-Elipe, J. Phys. D: Appl. Phys., 42 (2009) 145305.

[50] M.J. Mayo, R.W. Siegel, A. Narayanasamy, W.D. Nix, J. Mater. Res., 5 (1990) 1073-1082.

[51] J. Xu, H. Ju, L. Yu, Vacuum, 103 (2014) 21-27.

[52] S. Hashimoto, A. Tanaka, Surf. Interface Anal., 34 (2002) 262-265.

[53] C.J. Howard, T.M. Sabine, F. Dickson, Acta Cryst. B, 47 (1991) 462-468.

[54] Powder Diffraction Files, Card No. 00-021-1272, Database Edition, International Center for Diffraction Data (ICDD), Newton Square, PA 19073-3273, USA, (2012).

[55] E. Rosencher, B. Vinter, Optoelectronics, Cambridge University Press, Cambridge, U.K., 2002.

[56] W.C. Oliver, G.M. Pharr, J. Mater. Res., 7 (1992) 1564-1583.

[57] S.M. Babulanam, T.S. Eriksson, G.A. Niklasson, C.G. Granqvist, Sol. Energ. Mater., 16 (1987) 347-363.

[58] V.P. Melnik, I.M. Khatsevych, Y.V. Goltvyanskyi, Ukr. J. Phys., 56 (2011) 534-540.

[59] A. Tselev, I.A. Luk'yanchuk, I.N. Ivanov, J.D. Budai, J.Z. Tischler, E. Strelcov, A. Kolmakov, S.V. Kalinin, Nano Lett., 10 (2010) 4409-4416.

[60] J. Wu, W. Huang, Q. Shi, J. Cai, D. Zhao, Y. Zhang, J. Yan, Appl. Surf. Sci., 268 (2013) 556-560.

[61] J.Y. Suh, R. Lopez, L.C. Feldman, R.F. Haglund, J. Appl. Phys., 96 (2004) 1209-1213.

[62] V.P. Melnik, I. Khatsevych, V. Kladko, A. Kuchuk, V. Nikirin, B. Romanyuk, Mater. Lett., 68 (2012) 215-217.

[63] M. Castriota, N. Epervrier, T. Barone, G. De Santo, E. Cazzanelli, Ionics, 13 (2007) 205-211.

[64] E. Penilla, J. Wang, J. Nanomater., (2008).

[65] E. Penilla, F.G. Pérez-Gutiérrez, W. Duvall, G. Aguilar, J. Wang, Thin Solid Films, 524 (2012) 272-277.

[66] M.G. Krishna, A.K. Bhattacharya, Mater. Sci. Eng. B, 49 (1997) 166-171.

[67] R. Li, L. Bao, X. Li, CrystEngComm, 13 (2011) 5858-5862.

[68] R. Li, X. Tao, X. Li, J. Mater. Chem., 19 (2009) 983-987.

[69] H.J. Franek, G.H. Frischat, H. Knoedler, Glastechnische Berichte, 56 (1983).

[70] B. Grambow, Corrosion of Glass, in: R.W. Revie (Ed.) Uhlig's Corrosion Handbook, John Wiley & Sons, Inc., New York, NY, 2011, pp. 408.

[71] Powder Diffraction Files, Card No. 00-024-1157, Database Edition, International Center for Diffraction Data (ICDD), Newton Square, PA 19073-3273, USA, (2012).

[72] D.D. Wagman, W.H. Evans, V.B. Parker, R.H. Schumm, I. Halow, S.M. Bailey, K.L. Churney, R.L. Nuttall, J. Phys. Chem. Ref. Data, 11, Suppl. 2 (1982).

[73] NTUF, XL830 TEM Sample Preparation (Liftout) Guide, University of Washington, https://depts.washington.edu/ntuf/facility/training.html, (2013).

[74] H.-N. Cui, V. Teixeira, L.-J. Meng, R. Wang, J.-Y. Gao, E. Fortunato, Thin Solid Films, 516 (2008) 1484-1488.

[75] H. Zhang, Z. Wu, X. Wu, W. Yang, Y. Jiang, Vacuum, 104 (2014) 47-50.

[76] M. Gurvitch, S. Luryi, A. Polyakov, A. Shabalov, M. Dudley, G. Wang, S. Ge, V. Yakovlev, J. Appl. Phys., 102 (2007) 033504.

[77] L. Song, Y. Zhang, W. Huang, Q. Shi, D. Li, Y. Zhang, Y. Xu, Mater. Res. Bull., 48 (2013) 2268-2271.

[78] Z. Zhang, Y. Gao, H. Luo, L. Kang, Z. Chen, J. Du, M. Kanehira, Y. Zhang, Z.L. Wang, Energ. Environ. Sci., 4 (2011) 4290-4297.

[79] V.R. Morrison, R.P. Chatelain, K.L. Tiwari, A. Hendaoui, A. Bruhács, M. Chaker, B.J. Siwick, Science, 346 (2014) 445-448.

[80] H.A. Schaeffer, Materiały Ceramiczne, 64 (2012) 156-161.

[81] V. Belostotsky, J. Non-Cryst. Solids, 356 (2010) 129-131.

[82] M.J. Miller, J. Wang, Mat. Sci. Eng. B, 200 (2015) 50-58.

[83] E. Hryha, E. Rutqvist, L. Nyborg, Surf. Interface Anal., 44 (2012) 1022-1025.

[84] L.T. Sharpe, A. Stockman, W. Jagla, H. Jägle, J. Vis., 5 (2005).

[85] ASTM G173-03, Annual Book of ASTM Standards, Vol. 14-04, American Society for Testing and Materials, Philadelphia, PA, USA, https://rredc.nrel.gov/solar/spectra/am1.5.

[86] X. Cao, N. Wang, J.Y. Law, S.C.J. Loo, S. Magdassi, Y. Long, Langmuir, 30 (2014) 1710-1715.

[87] T. Bald, T. Quast, J. Landsberg, M. Rogava, N. Glodde, D. Lopez-Ramos, J. Kohlmeyer, S. Riesenberg, D. van den Boorn-Konijnenberg, C. Homig-Holzel, R. Reuten, B. Schadow, H. Weighardt, D. Wenzel, I. Helfrich, D. Schadendorf, W. Bloch, M.E. Bianchi, C. Lugassy, R.L. Barnhill, M. Koch, B.K. Fleischmann, I. Forster, W. Kastenmuller, W. Kolanus, M. Holzel, E. Gaffal, T. Tuting, Nature, 507 (2014) 109-113.

[88] Powder Diffraction Files, Card No. 00-044-0253, Database Edition, International Center for Diffraction Data (ICDD), Newton Square, PA 19073-3273, USA, (2012).

[89] A.L. Patterson, Phys. Rev., 56 (1939) 978-982.

[90] Bruker, General Area Detector Diffraction System (GADDS) User Manual, 4.1 (2005).

[91] L.A. Ladd, W. Paul, Solid State Commun., 7 (1969) 425-428.

[92] P.F. Bongers, Solid State Commun., 3 (1965) 275-277.

[93] J. Cao, E. Ertekin, V. Srinivasan, W. Fan, S. Huang, H. Zheng, J.W.L. Yim, D.R. Khanal, D.F. Ogletree, J.C. Grossman, J. Wu, Nat. Nano, 4 (2009) 732-737.

[94] N.R. Mlyuka, G.A. Niklasson, C.G. Granqvist, Sol. Energy Mater. Sol. Cells, 93 (2009) 1685-1687.

[95] R.J. Martín-Palma, J. Nanophoton., 3 (2009) 030305.

[96] M. Reidinger, M. Rydzek, C. Scherdel, M. Arduini-Schuster, J. Manara, Thin Solid Films, 517 (2009) 3096-3099.

[97] J. A. Woollam Co., Inc., CompleteEASE Version 4.63, (2011), www.jawoollam.com.

[98] Software Spectra, Inc., TFCalc Version 3.5, (2009), www.sspectra.com/support.

[99] M.J. Miller, J. Wang, Vacuum, 120, Part A (2015) 155-161.

[100] K.Y. Tsai, F.-H. Wu, H.-P.D. Shieh, T.-S. Chin, Mater. Chem. Phys., 96 (2006) 331-336.

[101] K.S. Karimov, M. Mahroof-Tahir, M. Saleem, M.T.S. Chani, A.K. Niaz, J. Semicon., 36 (2015) 073004.

[102] A.W. Smith, Appl. Phys. Lett., 23 (1973) 437-438.

Appendix A. UV-Vis-NIR Spectrophotometry Characterizations

The purpose of this appendix is to briefly describe how heated UV-Vis-NIR spectrophotometry characterizations were performed in this dissertation. The instrument used was a Varian Cary 5000 spectrophotometer, which is equipped with a dual cell Peltier temperature-controlled sample holder. This instrument is located in the core instrumentation of the Chemistry Department. An image of the Varian Cary 5000 is shown in Fig. A.1. Typically this device is used to characterize fluid samples which are held in cuvettes that fit conveniently into the cell holders. In this dissertation, it was desired to characterize the optical properties of thin solid films on substrates, and therefore the cuvette holders could not directly accommodate this material configuration. To overcome this challenge, sample mounting plates were fabricated that could be placed on the outside of the cuvette holders. The desired samples were then placed on these mounting plates and then characterized following the same approach as a cuvette sample would normally be characterized. The non-standard portion of the measurement is described in the following paragraph.

Fig. A.1. Varian Cary 5000 UV-Vis-NIR spectrophotometer with dual cell Peltier temperature-controlled sample holder.

To perform a heated spectrometry characterization using this apparatus, first place the sample mounting plates on the cuvette cell holders, as shown in Fig. A.2(a). Next, scan the baseline using the standard approach with the Varian Cary software. Remove the mounting plate near the front of the spectrometer (shown on the left side of Fig. A.2(a)). Mount the sample on the plate as shown in Fig. A.2(b). Return the mounting plate to the cell holder and then close the sample compartment. Set the desired temperature with the Peltier controller and perform the transmittance measurements using the standard approach.

Fig. A.2. (a) Peltier temperature-controlled cell holders with sample mounting plates attached. (b) Mounting plate with sample attached for characterization.

Appendix B. Matlab Code for Luminous Transmittance

```
% This Matlab code calculates luminous transmittance by integrating measured
transmittance with respect to the luminous efficiency reported by: L.T.
Sharpe, A. Stockman, W. Jagla, H. Jägle, J. Vis., 5 (2005).

clear all

% The l array shown below is the luminous efficiency reported by Sharpe et
al. (2005).

l =
[7.05E-07     9.51E-06     1.68E-04     3.90E-03     7.52E-02     4.90E-01
7.47E-07     1.01E-05     1.80E-04     4.20E-03     7.98E-02     5.03E-01
7.91E-07     1.08E-05     1.93E-04     4.51E-03     8.47E-02     5.17E-01
8.39E-07     1.15E-05     2.07E-04     4.85E-03     8.98E-02     5.31E-01
8.89E-07     1.23E-05     2.22E-04     5.22E-03     9.52E-02     5.45E-01
9.42E-07     1.31E-05     2.38E-04     5.61E-03     1.01E-01     5.58E-01
9.99E-07     1.40E-05     2.56E-04     6.03E-03     1.07E-01     5.72E-01
1.06E-06     1.49E-05     2.75E-04     6.48E-03     1.13E-01     5.86E-01
1.12E-06     1.59E-05     2.96E-04     6.96E-03     1.19E-01     6.00E-01
1.19E-06     1.69E-05     3.18E-04     7.48E-03     1.26E-01     6.14E-01
1.26E-06     1.80E-05     3.42E-04     8.05E-03     1.33E-01     6.27E-01
1.34E-06     1.92E-05     3.67E-04     8.66E-03     1.40E-01     6.40E-01
1.42E-06     2.05E-05     3.95E-04     9.33E-03     1.47E-01     6.53E-01
1.50E-06     2.19E-05     4.24E-04     1.01E-02     1.55E-01     6.66E-01
1.60E-06     2.34E-05     4.56E-04     1.09E-02     1.62E-01     6.79E-01
1.69E-06     2.50E-05     4.90E-04     1.17E-02     1.70E-01     6.92E-01
1.80E-06     2.68E-05     5.26E-04     1.26E-02     1.78E-01     7.05E-01
1.91E-06     2.86E-05     5.65E-04     1.36E-02     1.86E-01     7.17E-01
2.03E-06     3.06E-05     6.08E-04     1.46E-02     1.94E-01     7.30E-01
2.15E-06     3.26E-05     6.54E-04     1.57E-02     2.03E-01     7.42E-01
2.29E-06     3.49E-05     7.03E-04     1.68E-02     2.12E-01     7.54E-01
2.43E-06     3.73E-05     7.57E-04     1.81E-02     2.22E-01     7.66E-01
2.58E-06     3.98E-05     8.15E-04     1.94E-02     2.31E-01     7.78E-01
2.75E-06     4.26E-05     8.78E-04     2.08E-02     2.42E-01     7.90E-01
2.92E-06     4.55E-05     9.45E-04     2.23E-02     2.52E-01     8.01E-01
3.11E-06     4.87E-05     1.02E-03     2.39E-02     2.63E-01     8.12E-01
3.30E-06     5.21E-05     1.09E-03     2.55E-02     2.74E-01     8.22E-01
3.51E-06     5.58E-05     1.18E-03     2.73E-02     2.86E-01     8.32E-01
3.73E-06     5.97E-05     1.27E-03     2.92E-02     2.98E-01     8.42E-01
3.96E-06     6.39E-05     1.37E-03     3.12E-02     3.10E-01     8.50E-01
4.21E-06     6.83E-05     1.47E-03     3.33E-02     3.23E-01     8.59E-01
4.48E-06     7.31E-05     1.59E-03     3.56E-02     3.36E-01     8.66E-01
4.76E-06     7.83E-05     1.71E-03     3.80E-02     3.48E-01     8.74E-01
5.07E-06     8.38E-05     1.85E-03     4.05E-02     3.61E-01     8.81E-01
5.39E-06     8.97E-05     2.00E-03     4.32E-02     3.73E-01     8.88E-01
5.74E-06     9.61E-05     2.15E-03     4.60E-02     3.86E-01     8.96E-01
6.11E-06     1.03E-04     2.32E-03     4.90E-02     3.98E-01     9.05E-01
6.51E-06     1.10E-04     2.51E-03     5.22E-02     4.10E-01     9.15E-01
6.93E-06     1.18E-04     2.70E-03     5.55E-02     4.23E-01     9.24E-01
7.38E-06     1.27E-04     2.91E-03     5.90E-02     4.36E-01     9.34E-01
7.86E-06     1.36E-04     3.13E-03     6.28E-02     4.49E-01     9.42E-01
8.38E-06     1.46E-04     3.37E-03     6.67E-02     4.62E-01     9.50E-01
8.93E-06     1.57E-04     3.63E-03     7.09E-02     4.76E-01     9.57E-01
```

```
9.63E-01      9.62E-01      5.20E-01      1.74E-01      6.18E-02      1.66E-02
9.68E-01      9.54E-01      5.01E-01      1.68E-01      6.03E-02      1.55E-02
9.73E-01      9.46E-01      4.82E-01      1.63E-01      5.89E-02      1.43E-02
9.78E-01      9.37E-01      4.64E-01      1.58E-01      5.74E-02      1.32E-02
9.82E-01      9.27E-01      4.45E-01      1.54E-01      5.61E-02      1.21E-02
9.85E-01      9.17E-01      4.28E-01      1.49E-01      5.47E-02      1.11E-02
9.88E-01      9.07E-01      4.11E-01      1.44E-01      5.33E-02      1.01E-02
9.90E-01      8.98E-01      3.94E-01      1.39E-01      5.19E-02      9.08E-03
9.92E-01      8.88E-01      3.78E-01      1.35E-01      5.03E-02      8.14E-03
9.94E-01      8.78E-01      3.63E-01      1.30E-01      4.87E-02      7.25E-03
9.95E-01      8.68E-01      3.48E-01      1.25E-01      4.70E-02      6.42E-03
9.96E-01      8.58E-01      3.34E-01      1.20E-01      4.52E-02      5.66E-03
9.97E-01      8.46E-01      3.21E-01      1.16E-01      4.34E-02      4.97E-03
9.98E-01      8.34E-01      3.09E-01      1.11E-01      4.16E-02      4.35E-03
9.99E-01      8.21E-01      2.96E-01      1.06E-01      3.98E-02      3.80E-03
1.00E+00      8.08E-01      2.85E-01      1.01E-01      3.81E-02      3.30E-03
1.00E+00      7.95E-01      2.74E-01      9.69E-02      3.64E-02      2.85E-03
9.99E-01      7.81E-01      2.64E-01      9.27E-02      3.48E-02      2.45E-03
9.98E-01      7.66E-01      2.55E-01      8.87E-02      3.32E-02      2.10E-03
9.96E-01      7.51E-01      2.46E-01      8.51E-02      3.17E-02      1.78E-03
9.93E-01      7.35E-01      2.38E-01      8.20E-02      3.02E-02      1.50E-03
9.91E-01      7.18E-01      2.31E-01      7.91E-02      2.87E-02      1.27E-03
9.89E-01      7.00E-01      2.24E-01      7.66E-02      2.74E-02      1.06E-03
9.88E-01      6.81E-01      2.18E-01      7.44E-02      2.61E-02      8.84E-04
9.86E-01      6.61E-01      2.12E-01      7.24E-02      2.49E-02      7.34E-04
9.85E-01      6.41E-01      2.06E-01      7.06E-02      2.37E-02      6.08E-04
9.84E-01      6.21E-01      2.01E-01      6.90E-02      2.26E-02      5.03E-04
9.81E-01      6.00E-01      1.95E-01      6.76E-02      2.14E-02      4.15E-4];
9.78E-01      5.80E-01      1.90E-01      6.61E-02      2.03E-02
9.74E-01      5.60E-01      1.84E-01      6.47E-02      1.91E-02
9.68E-01      5.40E-01      1.79E-01      6.33E-02      1.79E-02

dL = 1.; % Incremental wavelength in nm

%************************************************************************
j = size(l);
numRows = j(1, 1);
denominator = 0.;
for i = 1:numRows       % This code integrates l to produce the denominator
    d(i, 1) = l(i,1)*dL;
    denominator = denominator + d(i,1);
end
%************************************************************************

data = [];  % Enter transmittance per nm measured from 830 to 390 nm

j = size(data);
numRows = j(1, 1);
numerator = 0.;
for i = 1:numRows       % This code integrates data to produce the numerator
n(i, 1) = d(i,1)*data(i,1);
    numerator = numerator + n(i,1);
end
numerator = numerator/100.;
Tlum = numerator/denominator     % Tlum is the desired luminous transmittance

wave =
```

```
[830     774     718     662     606     550     494     438
829     773     717     661     605     549     493     437
828     772     716     660     604     548     492     436
827     771     715     659     603     547     491     435
826     770     714     658     602     546     490     434
825     769     713     657     601     545     489     433
824     768     712     656     600     544     488     432
823     767     711     655     599     543     487     431
822     766     710     654     598     542     486     430
821     765     709     653     597     541     485     429
820     764     708     652     596     540     484     428
819     763     707     651     595     539     483     427
818     762     706     650     594     538     482     426
817     761     705     649     593     537     481     425
816     760     704     648     592     536     480     424
815     759     703     647     591     535     479     423
814     758     702     646     590     534     478     422
813     757     701     645     589     533     477     421
812     756     700     644     588     532     476     420
811     755     699     643     587     531     475     419
810     754     698     642     586     530     474     418
809     753     697     641     585     529     473     417
808     752     696     640     584     528     472     416
807     751     695     639     583     527     471     415
806     750     694     638     582     526     470     414
805     749     693     637     581     525     469     413
804     748     692     636     580     524     468     412
803     747     691     635     579     523     467     411
802     746     690     634     578     522     466     410
801     745     689     633     577     521     465     409
800     744     688     632     576     520     464     408
799     743     687     631     575     519     463     407
798     742     686     630     574     518     462     406
797     741     685     629     573     517     461     405
796     740     684     628     572     516     460     404
795     739     683     627     571     515     459     403
794     738     682     626     570     514     458     402
793     737     681     625     569     513     457     401
792     736     680     624     568     512     456     400
791     735     679     623     567     511     455     399
790     734     678     622     566     510     454     398
789     733     677     621     565     509     453     397
788     732     676     620     564     508     452     396
787     731     675     619     563     507     451     395
786     730     674     618     562     506     450     394
785     729     673     617     561     505     449     393
784     728     672     616     560     504     448     392
783     727     671     615     559     503     447     391
782     726     670     614     558     502     446     390];
781     725     669     613     557     501     445
780     724     668     612     556     500     444
779     723     667     611     555     499     443
778     722     666     610     554     498     442
777     721     665     609     553     497     441
776     720     664     608     552     496     440
775     719     663     607     551     495     439
```

```
figure(1);      % Plot luminous efficiency function from Sharpe et al. (2005)
plot(wave,l,'k-.', 'LineWidth', 1.5)

figure(2);        % Plot measured transmittance in visible region
plot(wave,data, 'k-..', 'LineWidth', 1.5)
```

Biography

Mark J. Miller received BS and MS degrees in Mechanical Engineering from Kansas State University in 2008 and 2010, respectively. During his MS program, he worked with Prof. Jack Xin on a computational project in which he modeled food-freezing processes with an interest in energy efficiency. In the summer of 2010, he taught English in Guatemala for fifth graders. After completing the MS program, Mark worked briefly for Caterpillar Inc. and then relocated to Seattle to begin a PhD program in Prof. Junlan Wang's Nanomechanics Lab. While at the University of Washington, Mark was awarded a Clean Energy Institute Graduate Fellowship and the Mark and Lisa Tuttle Endowed Fellowship in Mechanical Engineering. He mentored three undergraduate students and was a teaching assistant for four courses. Among several responsibilities, he maintained an Orion 5 UHV magnetron sputtering system for 4.5 years. He published three journal articles (see References Section) and has a fourth under review as of the publication of this dissertation. After completing his PhD, Mark plans to work as a D1C Process Engineer for Intel Corporation in Hillsboro, OR.